Impact of the coating on the insertion of magnetite nanoparticles into membrane models

Viviana B. Daboin[†], Candelaria I. Cámara[†], Jorge G. Uranga[†], Paula G. Bercoff[‡], Julieta S. Riva[†]*
*julieta.riva@unc.edu.ar

[†] CONICET, Instituto de Investigaciones en Fisicoquímica de Córdoba (INFIQC). Universidad Nacional de Córdoba, Facultad de Ciencias Químicas, Ciudad Universitaria, X5000HUA Córdoba, Argentina.
[‡] CONICET, Instituto de Física Enrique Gaviola (IFEG). Universidad Nacional de Córdoba, Facultad de Matemática, Astronomía, Física y Computación, Ciudad Universitaria, X5000HUA Córdoba, Argentina.

Keywords: Magnetite nanoparticles, Langmuir monolayer, maximum insertion pressure

ABSTRACT

In this study, we investigated the interactions between magnetite (Fe_3O_4) functionalized with either citrate (Fe_3O_4@C) or polyethyl-amino-ethyl cellulose (Fe_3O_4@PQ) and membrane model systems, using Langmuir isotherms and incorporation experiments. Phospholipid monolayers of 1,2-distearoyl-sn-glycero-3-phosphocholine (DSPC) and 1,2–distearoyl–sn–glycerol–3–phosphate (DSPA), which have the same hydrocarbon chains, were employed as cell membrane models. Magnetite nanoparticles (NPs) were successfully synthesized and characterized by transmission electron microscopy (TEM), X-ray diffraction (XRD), vibrating sample magnetometry (VSM), Fourier-transform infrared spectroscopy (FTIR), and zeta potential analyses. Both surface pressure vs. time incorporation experiments and compression isotherms revealed favorable interactions between the NPs and the lipid monolayers. We also evaluated the influence of the initial surface pressure of the monolayer to determine the maximum insertion pressure (MIP). At low concentrations, the NPs with both types of coatings expanded the monolayers due to area exclusion effects, while at higher concentrations, they promoted the formation of 3D structures. Fe_3O_4@PQ exhibited stronger initial interactions with the lipid films, particularly with DSPC, likely due to enhanced hydrophobic and electrostatic interactions. However, Brewster angle microscopy imaging and insertion experiments revealed that Fe_3O_4@C penetrate more effectively into the monolayers. In addition, the impact of using fresh versus aged NP dispersions was assessed. Aged NP dispersions caused greater structural disruption and reduced film rigidity, underscoring the importance of using fresh nanoparticle suspensions to ensure reproducibility. All systems displayed MIP values above 30 mN/m, exceeding physiological membrane pressures and suggesting that the NPs with both types of coatings are capable of penetrating biological membranes. Overall, Fe_3O_4@C demonstrated higher insertion efficiency and time-dependent penetration rate values (V_{MAX}) under all conditions, highlighting the crucial role of surface chemistry in modulating nanoparticle–membrane interactions. These observations emphasize the significant role of nanoparticle surface chemistry in modulating the structural organization of phospholipid monolayers.

INTRODUCTION

Magnetic nanoparticles (NPs) have emerged as versatile tools for a wide range of biomedical applications, including hyperthermia treatment, magnetic resonance imaging (MRI), and drug delivery systems. Functionalizing NPs with organic and inorganic materials is crucial for these applications. Different types of NPs have been coated with proteins, silica, polymers, surfactants, and various organic compounds to enhance their biocompatibility and functionality. These coatings help reduce toxicity and improve their

performance, particularly in drug delivery applications.[1,2]

Citrate and cellulose derivatives are some of the commonly used materials for NP functionalization to enhance their biocompatibility and stability in biological fluids. Citrate coating increases the hydrophilicity of NPs due to the presence of free carboxyl groups, which impart a negative surface charge, making the particles hydrophilic. This property may positively impact in their performance in drug delivery systems.[3] On the other hand, NPs coated with macromolecules, such as cellulose-derived biopolymers, have also been widely studied.[4] This type of coating improves biocompatibility and stability, provides functional groups (-NH_2 and -OH) for further functionalization and drug attachment, and enhances hydrophilicity. Additionally, cellulose-based coatings are particularly suitable for drug delivery applications, and they are widely used as non-viral gene delivery systems.[5]

Transporting NPs across cell membranes is crucial for developing innovative therapeutic agents. However, understanding the underlying mechanisms remains challenging due to the complexity of the process. *In vivo* studies have demonstrated that factors such as NP shape, size, and surface properties, including charge density and surface charge, play a significant role in their internalization into cells.[6] A valuable alternative to *in vivo* experiments for studying molecular interactions with cell membranes is the use of model membranes. These models can be generated using various methods, with the most commonly employed systems being planar bilayer lipid membranes, liposomes, and lipid monolayers.[6,7]

In this context, Langmuir monolayers (two-dimensional films formed by the adsorption of amphiphilic molecules at the air-water interface) are commonly used to investigate the assembly and properties of phospholipids and surfactants.[7] Many studies have analyzed the interactions between biological membrane models and various molecules, including peptides,[8] proteins,[9,10] polymers,[11,12] and drugs.[13] Particularly, the Langmuir monolayer technique has emerged as a powerful tool for studying interactions between functionalized nanoparticles and phospholipid monolayers.[14-21] For example, Piosik et al. investigated the interaction of chitosan-coated Fe_3O_4 nanoparticles with 1,2-dipalmitoyl-sn-glycero-3-phosphocholine (DPPC) monolayers as a membrane model. From Langmuir isotherms, they concluded that hybrid films composed of DPPC and Fe_3O_4-chitosan are less stable than pure DPPC films.[16,17] They also found that the number of adsorbed or incorporated NPs can be regulated at a surface pressure of $\pi = 35$ mN/m by adjusting their concentration near the membrane. This suggests that the amount of drugs and biomolecules transferred into cells can be controlled by the number of transported Fe_3O_4-aminated chitosan nanoparticles, highlighting the potential of chitosan-functionalized NPs as carriers for delivering bioactive materials to biological cells. More recently, in a different paper, the same authors evaluated the effect of functionalizing NPs with chitosan, PVA, and their blend on model cell membranes composed of DPPC, using the Langmuir technique.[22] They demonstrated that the type of biocompatible polymer in the NP shell plays a crucial role in determining the effectiveness of the adsorption process into the model cell membrane. Specifically, their results showed that chitosan-coated NPs significantly enhance adsorption compared to poly(vinyl alcohol)-coated NPs.[22]

In our previous works we investigated the behavior of Fe_3O_4 NPs coated with polysaccharides chitosan and dextran at a liquid/liquid interface,[23] and the interaction of these particles with pharmaceutical drugs at a liquid/liquid interface[24,25] and a water/air interface;[14] we also studied their behavior in the presence of an external magnetic field.[26]

Here, we investigated how coating magnetite NPs with small molecules or macromolecules influences their interactions with phospholipid membranes, using compression isotherms made with either pure phospholipids or hybrid films composed of phospholipids and NPs, as well as

their insertion into membrane models through incorporation experiments. We used citrate and polyquaternium-10 (PQ-10) as coating agents, specifically Celquat SC-230, a high-molecular-weight polysaccharide containing quaternary ammonium groups, known for its hydrophilicity, biocompatibility, and mucoadhesive properties.[27,28]

In this study, we select distearoyl-sn-glycero-3-phosphocholine (DSPC) and 1,2-distearoyl-sn-glycero-3-phosphate (DSPA) as model phospholipids to investigate nanoparticle–monolayer interactions. These lipids share the same hydrocarbon chains but differ in their head group, providing a useful framework for studying the role of surface charge in interfacial phenomena. DSPA carries a net negative charge under physiological conditions, whereas DSPC is zwitterionic and overall neutral. This contrast enables controlled comparisons of electrostatic effects in simplified systems, an approach commonly employed in model membrane studies.[17,22]

The insights gained from these systems contribute to a deeper understanding of how magnetic NPs interact with charged versus neutral lipid environments, interactions that are relevant in biomedical contexts including drug delivery, nanotoxicology, and biosensing.[15] Therefore, in this work we aimed to investigate the interfacial behavior of Fe_3O_4@C and Fe_3O_4@PQ NPs interacting with phospholipid monolayers as smembrane models. Additionally, we examined the impact of NP aging, comparing interactions using fresh vs. aged NP solutions, as magnetite NPs tend to aggregate over time. The findings of this study contribute to a deeper understanding of Fe_3O_4 NP interactions with model membranes, particularly regarding the influence of surface charge and colloidal stability under interfacial conditions.

EXPERIMENTAL SECTION

Materials

All reagents are commercially available and were used without further purification. Iron (II) chloride tetrahydrate and Iron (III) chloride hexahydrate were purchased from Alfa Aesar. Ammonium hydroxide (NH_4OH) and Sodium citrate 2-hydrate were purchased from Cicarelli. Polyquaternium 10, PQ-10: SC230, (600.000-2.000.000 g/mol) was acquired from The National Starch and Chemical Co. (Bridgewater, NJ). The phospholipids DSPA and DSPC (Scheme 1(a) and (b), respectively) were purchased from Avanti Polar Lipids (Alabaster, Al). NaCl (subphase electrolyte) was purchased from Sigma Aldrich (p.a. grade), Chloroform and Methanol were acquired from Dorwill. The phospholipid solutions were prepared in chloroform:methanol 2:1 v/v at a concentration value equal to 1.0 mM. Magnetite NP dispersion was prepared in ethyl alcohol, at a concentration of 1 mg/mL, and sonicated for 10 min before use.

Synthesis of Fe_3O_4 Nanoparticles

We used the co-precipitation method for the synthesis of magnetite, as reported in the literature.[23,29,30]. Briefly, 50 mL of $FeCl_2$ 0.2 M was mixed with 50 mL of $FeCl_3$ 0.4 M to obtain a molar ratio of 1:2 (Fe^{2+}:Fe^{3+}), and the resultant solution was stripped of O_2 with bubbling N_2. When the temperature reached 80 °C, a solution of 25% v/v NH_4OH was added dropwise with vigorous stirring until a pH = 9.00 was reached. The resulting black dispersion was kept at 80 °C for 1 h with vigorous stirring. The black precipitate obtained by decantation was then washed several times, and the as-synthesized magnetite was dried in an oven at 25 °C.

Coating of Fe_3O_4 NPs with citrate

The coating of Fe_3O_4 NPs with sodium citrate was carried out according to a procedure reported in another study.[31] In summary, 0.5 g of Fe_3O_4 NPs was dissolved in 100 mL of a 0.5 M trisodium citrate solution. The mixture was stirred magnetically under nitrogen gas at 80°C for 1 h. After cooling to room temperature, the resulting magnetic dispersion was precipitated with acetone to remove the excess citrate groups adsorbed on the NPs. They were then collected with a magnet

and dried at room temperature. The citrate-modified Fe_3O_4 NPs are referred to as Fe_3O_4@C. Scheme 1(c) shows a schematic representation of the sodium citrate-coated NPs.

Coating of Fe_3O_4 NPs with PQ-10

Briefly, 0.5 g of Fe_3O_4 NPs was dispersed in a 175 mL aqueous solution of PQ-10 for 12 h under continuous mechanical stirring, resulting in a stable NP suspension. Finally, the NPs were precipitated using a magnet and then they were dried at room temperature. These NPs were named Fe_3O_4@PQ, and Scheme 1(d) shows a schematic representation of them.

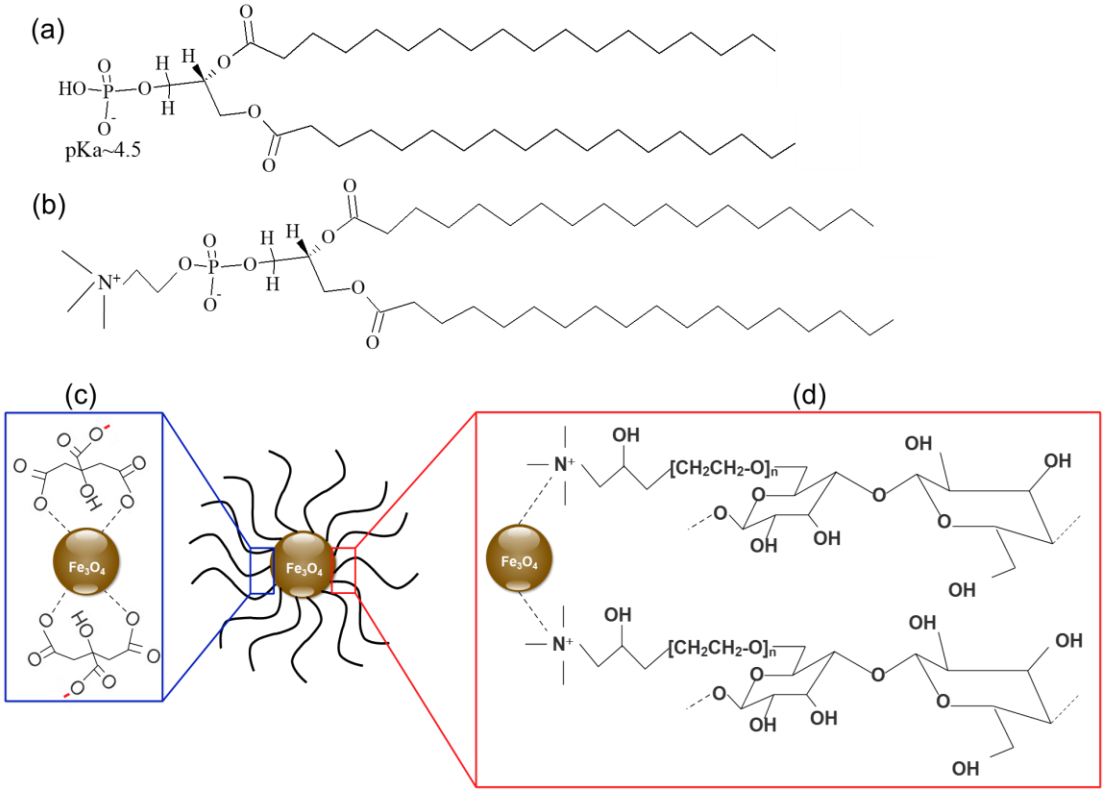

Scheme 1. Structure of (a) DSPA, (b) DSPC, (c) Fe_3O_4@C and (d) Fe_3O_4@PQ.

Characterization

Magnetite NPs with both types of coatings, Fe_3O_4@C and Fe_3O_4@PQ, were characterized using different techniques. A transmission electron microscope (HITACHI HT7800, operating at 120 kV) was used to determine the morphology of the NPs. The crystal structure was identified using X-ray powder diffraction (XRD) with a PANalytical X'Pert Pro diffractometer, operated in Bragg-Brentano geometry at 40 kV, 40 mA, with Cu Kα radiation (λ = 1.5418 Å) and a step size of 0.02°, over a 2θ range from 10° to 80°. Surface functionalization of the NPs was characterized by Fourier transform infrared spectroscopy (FTIR) using a Nicolet iN10 MX Instrument FTIR spectrometer. The zeta potential (ζ) of the samples was determined by electrophoretic light scattering (ELS) measurements using a Delsa Nano C instrument (Beckman Coulter). Aqueous dispersions of the NPs with both functionalizations (0.01 mg/mL in ethanol) were prepared and sonicated for 30 minutes. The measurements were performed in triplicate, and the electrophoretic mobilities were converted into ζ-potential values using the Smoluchowski equation. Magnetic measurements were performed in a Lakeshore 7300 vibrating-

sample magnetometer (VSM) at 300 K, with maximum applied fields of ±1.8 T.

Surface pressure–molecular area isotherms

The interactions between the NPs and the phospholipid monolayers were studied using a hydrophobic Teflon Langmuir trough (KSV Mini-Trough 36.4 cm x 7.5 cm, KSV model 2000). The Wilhelmy method with a platinum plate was used to monitor the surface pressure vs molecular area isotherms. The subphase consisted of a 10 mM NaCl electrolyte solution prepared with ultrapure Milli-Q deionized water, adjusted to pH 6.0. The temperature during the experiments was maintained between 23 and 25 °C by regulating the ambient conditions with air conditioning. The subphase temperature was monitored with a thermometer at the beginning and at the end of each experiment to ensure thermal stability.

Pure phospholipid monolayers (50 µL of DSPA or DSPC at 1.0 mM) or hybrid films (prepared by mixing 0.5, 1, 2, 4, 7, or 10 µL of NP suspension with 50 µL of phospholipid solution), whose structures are shown in Scheme 1(c) and (d), were spread onto the air/water interface using a microsyringe. After solvent evaporation (approximately 20 minutes), the monolayers were compressed at a constant rate of 10 mm/min while the surface pressure (π) was recorded automatically. The absence of surface-active impurities in the spreading solvent and subphase was verified prior to each experiment by confirming that the surface pressure was below 0.2 mN/m. All surface pressure–area isotherms were recorded in triplicate to ensure reproducibility. A schematic representation of the mixed monolayer formation is shown in Scheme 2(a).

Using the recorded π-A isotherms, the compressibility modulus can be calculated through the following equation:

$$Cs^{-1} = -A\left(\frac{\partial \pi}{\partial A}\right)_T \qquad (1)$$

where Cs^{-1} is the compressibility, reflecting variations in the in-plane elasticity of the monolayer, and π is the surface pressure measured at each area point (A) of the pressure-area isotherm.[25]

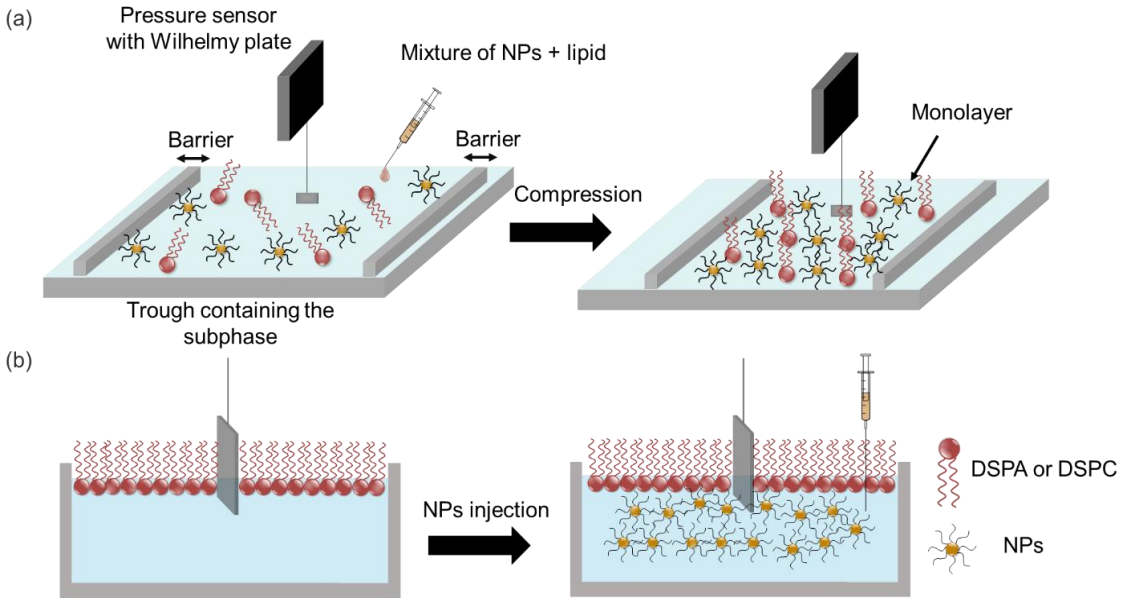

Scheme 2. Schematic representation of (a) surface pressure–area isotherm experiments and (b) insertion experiments.

Brewster angle microscopy (BAM)

The different monolayers were examined by Brewster angle microscopy (BAM) using an EP3 imaging ellipsometer (Accurion, Göttingen, Germany) equipped with a 20× objective (Nikon, NA 0.35, Tokyo, Japan). Before sample injection, the instrument was calibrated using the clean interface to determine the relationship between the images' average grey level (GL) and the reflected light intensity (RP). Image analysis and quantification were performed using the free software *ImageJ*. The average grey level was calculated from six different regions corresponding to each phase in at least two images for each condition. The reflected intensity (RP) of each image was calculated as the difference between the GL and the dark signal (DS, reflectivity value for the clean interface without lipid monolayer), multiplied by a calibration factor (CF), according to the following equation: RP = (GL – DS) × CF.[26,32]

Insertion experiments

Insertion experiments were conducted in a Teflon minitrough with a constant surface area (A = 15.8 cm²), filled with 5 mL of the solution used as the subphase. The subphase composition and temperature conditions were identical to those used for the surface pressure–area isotherm measurements: a 10 mM NaCl solution prepared with ultrapure Milli-Q water at pH 6.0, and temperature maintained at 24.0±0.5 °C.

First, we studied the adsorption of Fe_3O_4@C and Fe_3O_4@PQ on DSPA and DSPC monolayers as a function of the injected NPs concentration, allowing the determination of the saturation concentration. This value corresponds to the concentration above which no further increase in surface pressure is observed. For this purpose, the DSPC or DSPA monolayer was formed at 15 mN/m (in the liquid-expanded phase), and a specific amount of NPs was injected beneath the lipid monolayer, as shown in Scheme 2(b). The initial surface pressure (π_i) was recorded prior to injection, and the final surface pressure (π_f) was measured once the system reached equilibrium (~30 minutes). The change in surface pressure ($\Delta\pi = \pi_f - \pi_i$) as a function of NP concentration typically follows a hyperbolic trend and it was fitted using the following equation:[32]

$$\Delta\pi = \frac{(\Delta\pi_{max} C)}{(K_{0.5}+C)} \quad (2)$$

where C is the nanoparticle concentration, $\Delta\pi_{max}$ is the maximum change in surface pressure induced by the NPs, and $K_{0.5}$ represents the NP concentration required to reach half of $\Delta\pi_{max}$.

Knowing the saturation concentration, the influence of the monolayer packing upon NP insertion was evaluated. For this, the same Teflon minitrough, subphase, and temperature conditions were used. Phospholipid solutions were spread at the air–water interface to obtain initial surface pressures (π_i) ranging from 8 to 30 mN/m. A fixed concentration of NPs (Fe_3O_4@C or Fe_3O_4@PQ) was then injected beneath the monolayer, and the final surface pressure (πf) was recorded after ~20 minutes. Each injection was performed only after stabilization of the initial surface pressure, which typically occurred after between 3 and 5 minutes.

The variation in surface pressure after NP injection ($\Delta\pi = \pi f - \pi_i$) was plotted against the initial pressure (π_i), and the data were fitted linearly. The extrapolated intersection with the x-axis gives the maximum insertion pressure (MIP), a parameter that reflects the compatibility between the NPs and the lipid monolayer.[26,33]

The maximum incorporation rate (V_{max}) was determined for all the systems studied (NPs/DSPA or NPs/DSPC). V_{max} was obtained from the first derivative of the surface pressure (π) versus time curves, with the peak value corresponding to V_{max}. This analysis was performed across the full π_i range (8–30 mN/m), and the resulting V_{max} values were plotted as a function of π_i to assess the influence of monolayer packing on NP insertion dynamics.

To further characterize the insertion kinetics, the experimental π versus time curves were fitted using a first-order kinetic model, according to the following equation:

$$\pi(t) = \pi_0 + \Delta\pi_{max}(1 - e^{-kt}) \qquad (3)$$

where $\pi(t)$ is the surface pressure at time t, $\Delta\pi_{max}$ represents the amplitude of the surface pressure increase, k is the pseudo-first-order rate constant (s^{-1}), and π_0 is the initial surface pressure prior to NP injection.[34,35] In all cases, time zero ($t = 0$) was defined as the moment of NPs injection, following stabilization of the initial pressure. This kinetic analysis was performed for all the systems studied (NPs/DSPA and NPs/DSPC).

As previously described, Fe_3O_4 NPs were coated with citrate or PQ10 (Fe_3O_4@C and Fe_3O_4@PQ, respectively, as shown in Scheme 1). The obtained NPs were characterized by several techniques and they were further used to study their interactions with model cell membranes.

TEM images of as-prepared and functionalized Fe_3O_4 NPs are shown in Figure 1, where, it can be observed that the obtained particles are nearly spherical.

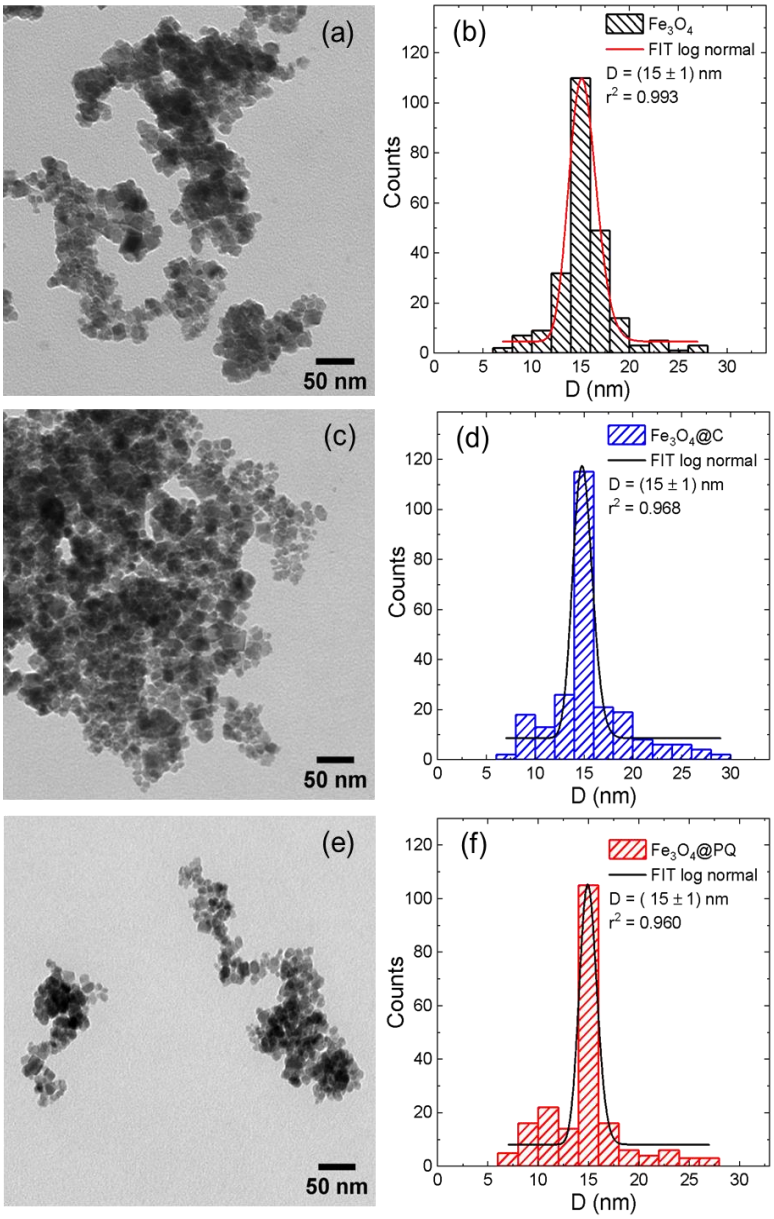

Figure 1. TEM image and corresponding size histogram of the as-prepared (a), (b) Fe_3O_4 NPs, and functionalized (c), (d) Fe_3O_4@C and (e), (f) Fe_3O_4@PQ NPs.

The average size of the NPs was determined from the analysis of multiple TEM images, and the corresponding size histograms are shown in Figure 1(b), (d), and (f), resulting in an approximate mean diameter of 15 nm for Fe_3O_4, Fe_3O_4@C, and Fe_3O_4@PQ. This indicates that the coating process does not significantly alter either the size or the morphology of the NPs.

The crystalline nature of Fe_3O_4, Fe_3O_4@C, and Fe_3O_4@PQ NPs was confirmed by XRD (Figure S1 in the Supplementary Information). The peak positions corresponding to the (111), (220), (311), (400), (422), (511), and (440) reflections, as well as their relative intensities, match the standard diffraction peaks of a cubic unit cell, which corresponds to the spinel magnetite structure (JCPDS 00-019-0629).[36]

The presence of both surface coatings on the synthesized NPs was confirmed by FTIR analysis, as shown in Figure 2(a). All spectra exhibit three absorption bands around 630, 590, and 450 cm^{-1} indicating the formation of magnetite. The bands at 590 and 450 cm^{-1} correspond to the stretching vibrations of Fe-O in the tetrahedral and octahedral sites, respectively. Additionally, the bands in the region of 3420 cm^{-1} and 1635 cm^{-1} can be attributed to the stretching and bending vibrations of hydroxyl groups present on the surface of magnetite NPs.[37,38]

In Fe_3O_4@C, bands appear at 1400, 1260, and 1050 cm^{-1} corresponding to the symmetric stretching of COO-, the symmetric stretching of C-O, and the OH group of sodium citrate, respectively. In addition, the band at 1630 cm^{-1} is typically associated with the asymmetric stretching of COO- and the band at 3400 cm^{-1} with the O-H groups of citrate.[39-42]

The spectrum of PQ-coated magnetite NPs (Fe_3O_4@PQ) shows bands in the 3000-2800 cm^{-1} region, attributed to the symmetric and asymmetric stretching modes of C–H in methyl (CH_3) and methylene (CH_2) functional groups. At 1490 cm^{-1}, a vibrational band corresponding to the stretching of the quaternary ammonium portion of polyquaternium is observed. Bands in the 1200-950 cm^{-1} region are primarily associated with the stretching modes of carbohydrate rings and the side groups (C–O, C–OH and C–H).[42-44]

The surface charge of the coated NPs was assessed through zeta potential measurements. The suspension of Fe_3O_4@C exhibited a moderately negative surface potential of -3 mV, whereas for Fe_3O_4@PQ, the zeta potential values were positive, 6 mV.

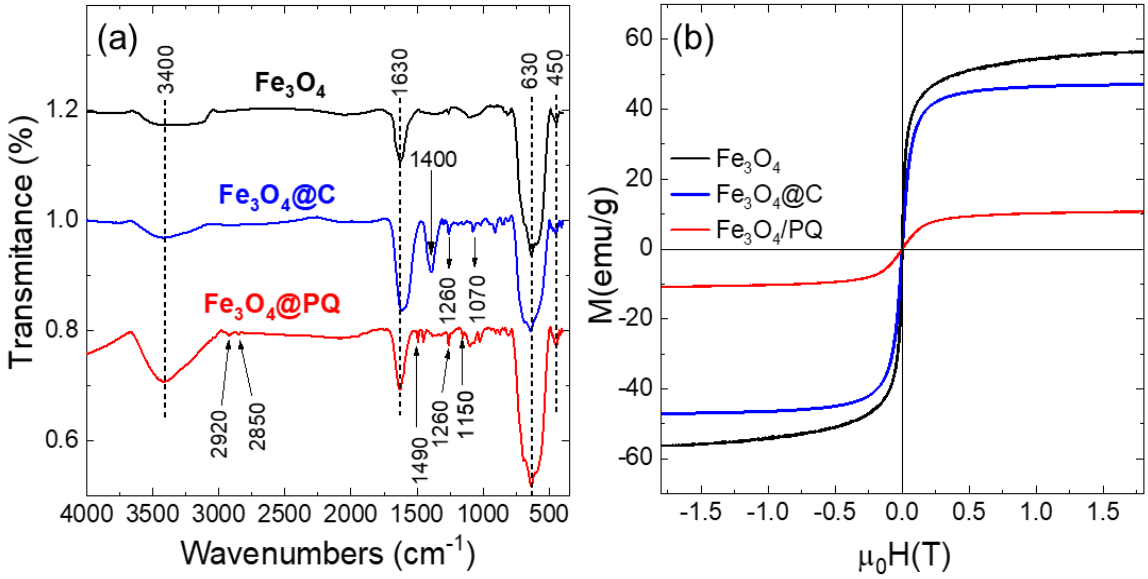

Figure 2. (a) FTIR spectra and (b) magnetic hysteresis loops of Fe_3O_4, Fe_3O_4@C and Fe_3O_4@PQ.

Figure 2(b) shows the magnetization M versus applied field H hysteresis loops of Fe_3O_4, Fe_3O_4@C and Fe_3O_4@PQ NPs, measured at 300 K. Superparamagnetic behavior is observed in all samples, as remanence (M_R) and coercivity (H_C) values are nearly negligible in the absence of an external magnetic field. Since the maximum applied field of 1.8 T was not enough to saturate the samples, the M_S values were estimated using two methods: (1) the law of approach to saturation, $M = M_S + b/H$, where b is a constant, and (2) the y-intercept of the M vs $1/H$ plot.[45-47] Both calculations yielded the same results: 58 emu/g, 48 emu/g, and 11 emu/g for Fe_3O_4, Fe_3O_4@C and Fe_3O_4@PQ NPs, respectively. The Ms values of the coated NPs are lower than those of the bare NPs, which is attributed to the presence of the non-magnetic sodium citrate and PQ-10 coatings on the particle's surface.[48]

Surface Pressure–Mean Molecular Area Isotherms

To study the influence of Fe_3O_4@C and Fe_3O_4@PQ on the thermodynamic behavior of the DSPA and DSPC monolayers, mixtures of these functionalized NPs and phospholipids were spread over the electrolyte solution subphase and compressed at the air–water interface. During compression, the surface pressure (π) versus the mean molecular area (MMA) per phospholipid molecule isotherms (π-A isotherms) were recorded for NPs/DSPA and NPs/DSPC; these isotherms are presented in Figures 3 and 4, respectively. The hybrid films are denoted Fe_3O_4@C/DSPA, Fe_3O_4@PQ/DSPA, Fe_3O_4@C/DSPC and Fe_3O_4@PQ/DSPC. In the plots, the isotherms of pure DSPA or DSPC are included for comparison (black lines).

Bare NPs form Langmuir films exhibiting low surface pressure values, as can be seen in Figure S2 in the Supplementary Information. Particularly, the Fe_3O_4@PQ film reaches a surface pressure value of 25 mN/m, which is higher than the 17 mN/m recorded for the Fe_3O_4@C film.

Figures 3(a) and (b) show the isotherms of pure DSPA (black lines), which are consistent with those presented in the literature.[10,14] The extrapolated mean molecular area (A_{EXT}) value determined for the DSPA monolayer is 0.45 nm2. The DSPA isotherm exhibits a sharp slope in the region where surface pressure rises, suggesting an ordered chain state. Furthermore, Cs^{-1} reaches a value of 299 mN/m, which corresponds to the solid phase (Figures 3(c) and (d)). These observations confirm that the surface pressure increase observed in the isotherm is associated with the rapid enhancement of molecular packing density in the DSPA film and its transition to the solid state.

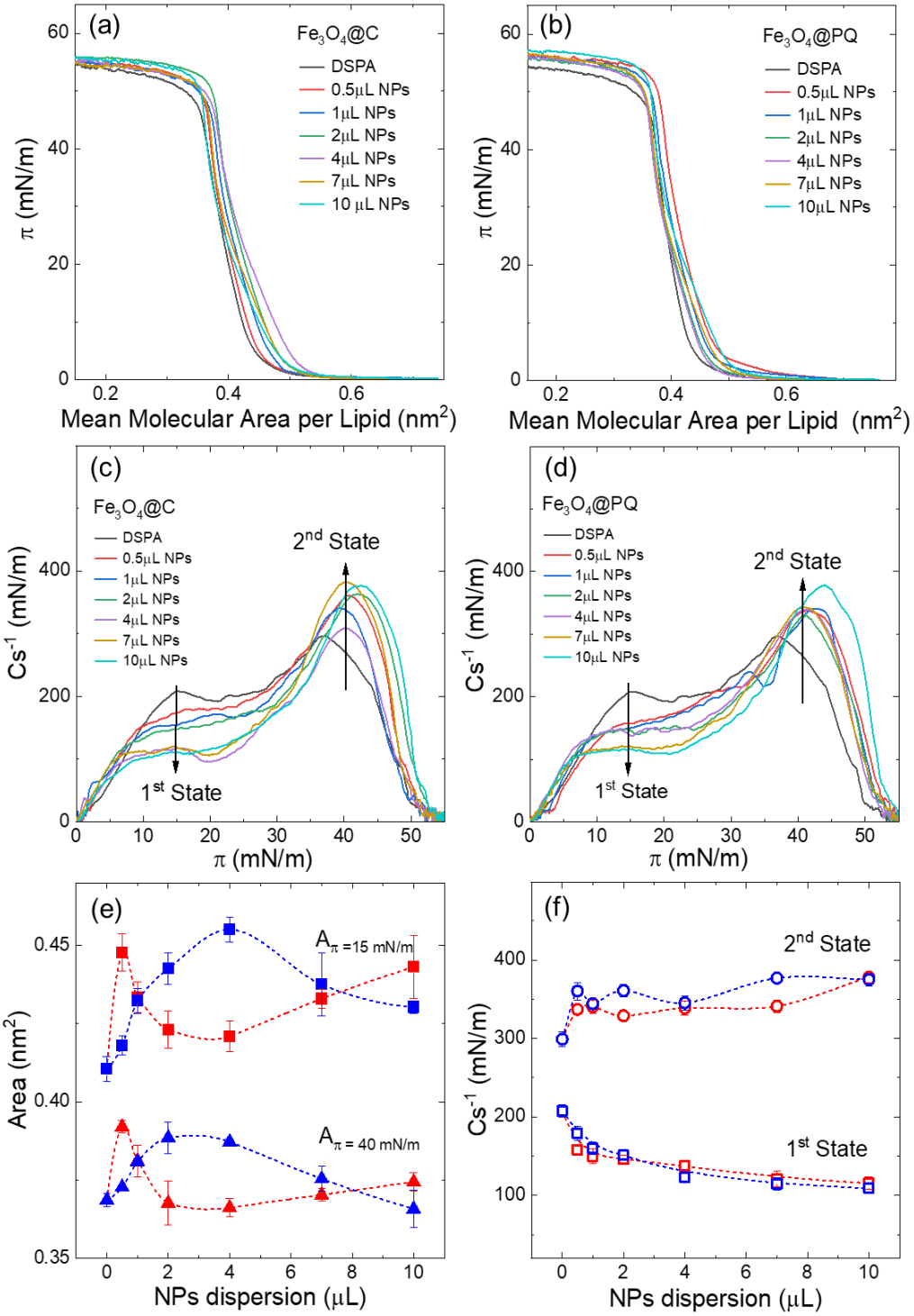

Figure 3. Surface pressure as a function of the mean molecular area per lipid and compressibility modulus for the hybrid films: (a), (c) Fe_3O_4@C/DSPA and (b), (d) Fe_3O_4@PQ/DSPA. (e) Mean molecular area as a function of the amount of NPs at two different surface pressures (15 mN/m and 40 mN/m) for Fe_3O_4@C (blue) and Fe_3O_4@PQ (red). (f) Maximum compressibility modulus (Cs^{-1}) of the NP dispersions for Fe_3O_4@C/DSPA (blue) and Fe_3O_4@PQ/DSPA (red) monolayers, in both LE and LC phases. Error bars represent standard deviations from triplicate measurements. In this figure, the error bars are smaller than the size of data points.

The presence of NPs in the monolayers alters the behavior of the π-A isotherms, and the shape varies with the NPs concentration in the monolayer. The incorporation of NPs into a DSPA monolayer results in two distinct behaviors depending on the NP concentration: (1) At low NP concentrations, the isotherm shifts to higher MMA values compared to the position of the pure DSPA isotherm, due to the area exclusion effect; and (2) at higher NP concentrations, while the area exclusion effect still occurs, its influence diminishes as the NP concentration increases.[15]

Particularly for Fe_3O_4@C/DSPA hybrid films, at π = 15 mN/m, the MMA occupied by a molecule increased until the addition of 4 μL of Fe_3O_4@C, resulting in a 10% increase compared to the area occupied by pure DSPA, as a consequence of the formation of a more fluidized monolayer. The changes of MMA with the amount of NPs at different surface pressures (15 mN/m and 40 mN/m) and critical pressure are summarized in Figure 3(e). The shift of the isotherms toward higher MMA per lipid is evident from the earlier onset in the mixed monolayers compared to pure DSPA. This phenomenon can be attributed to the presence of particles that take up a portion of the area available for the reorganization of the lipid molecules.[15]

However, the presence of more Fe_3O_4@C NPs produces a decrease in the MMA as a consequence of NP-NP interactions, which may promote the formation of rigid domains of solid particles. The isotherms formed with Fe_3O_4@PQ/DSPA follow the same trend than Fe_3O_4@C/DSPA, with the difference that with Fe_3O_4@PQ, the maximum shift of the isotherms towards greater MMAs than pure DSPA occurs with a lower amount of NPs (2 μL of NPs dispersion). After that, the addition of more NPs causes an isotherm shift towards lower molecular areas, obtaining isotherms similar to that of the pure lipid. This shift occurs because when the concentration of NPs exceeds a certain critical amount, 3D particle stackings are formed, which begin to accumulate on the pre-existing mixed monolayer, potentially resulting in the growth of out-of-plane structures, such as wrinkles, folds, or buckles. In this situation, the effective concentration of NPs at the interface is lower than that expected from the complete spreading of the NPs across the available area. Consequently, this leads to a diminished significance of the excluded area effects as the concentration of NPs increases. It is important to note that magnetite NPs tend to agglomerate due to their strong interaction. A similar behavior was found by Guzman et al. for carbon black particles on Langmuir monolayers of 1,2-dipalmitoyl-sn-glycero-3-phosphocholine (DPPC), due to the strong hydrophobic interaction between these kinds of NPs.[14]

The critical amount of NPs beyond which the isotherms shift due to particle stackings forming three-dimensional geometries is lower for Fe_3O_4@PQ than for Fe_3O_4@C, because of their distinct chemical properties. Although both types of particles are magnetic and tend to agglomerate, the presence of a positive charge on the surface of Fe_3O_4@PQ particles is neutralized by the negative charge of the DSPA, which promotes their agglomeration in the film. Additionally, the cellulose chain of the PQ exhibits stronger Van der Waals interactions with the lipid carbon chain, enhancing molecular stability and cohesion.

The compression modulus is shown in Figures 3(c) and 3(d), and the values are shown in Figure 3(f). Based on the criteria established by Davies and Rideal,[49] a monolayer is classified as liquid-expanded (LE, isotropic liquid) when $12.5 < Cs^{-1} < 50$ mN/m. The monolayer is considered to be in the liquid state when Cs^{-1} ranges from $50 < Cs^{-1} < 100$ mN/m, while the liquid-condensed (LC, liquid crystalline) phase occurs when $100 < Cs^{-1} < 250$ mN/m. Finally, the monolayer is categorized as a solid (S, 2D crystalline solid) when $Cs^{-1} > 250$ mN/m. The packing density of particles in a monolayer and the film's elasticity are indicated by the maximum value of the compression modulus. As observed, the compression modulus exhibits two maxima, one in a more expanded state, with π values between 10 and 20 mN/m, and

another at π values around 40-50 mN/m, indicating a more condensed state of the monolayer.

Figure 3(f) summarizes the Cs^{-1} values of these two states for NPs/DSPA films. The presence of NPs clearly decreases the degree of packing particles in the monolayer at the more expanded state. The lower the degree of condensation of the monolayer, the higher the concentration of NPs in the system. However, the Cs^{-1} shows the highest value at the more condensed state in hybrid films with respect to pure DSPA films. This suggests that, in the presence of nanoparticles, the hybrid film becomes less compressible at high surface pressures, indicating a more solid-like behavior compared to pure DSPA. Also, hybrid films present higher π values when the monolayer collapses (Figure 3(a) and (b)), indicating more stability of the hybrid films at higher surface tensions.

As shown in Figures 4(a) and 4 (b) (black lines), the isotherms of pure DSPC exhibit an increase in surface pressure during the transition from the gas phase to the condensed state, with an extrapolated mean molecular area (A_{EXT}) of approximately 0.51 nm^2, similar to the value previously reported by several authors.[16,50-52] The A_{EXT} value determined for the DSPC monolayer is, therefore, higher than that of the DSPA film (0.45 nm^2), revealing a lower molecular packing density in the initial compression stage of the DSPC Langmuir film compared to DSPA. However, the DSPC isotherms reach higher surface pressure values in the solid state, forming a more stable film. This behavior is attributed to the fact that, at the working pH, DSPA is negatively charged, whereas DSPC is zwitterionic. Since both lipids have identical hydrocarbon chain lengths and were studied under the same subphase conditions, the difference in behavior can be ascribed to the nature of the polar head group.

In addition, the maximum Cs^{-1} value measured for the DSPC monolayer is 230 mN/m, which is lower than that of DSPA (299 mN/m). Consequently, even in the final compression stage, the DSPC film remains notably less rigid.

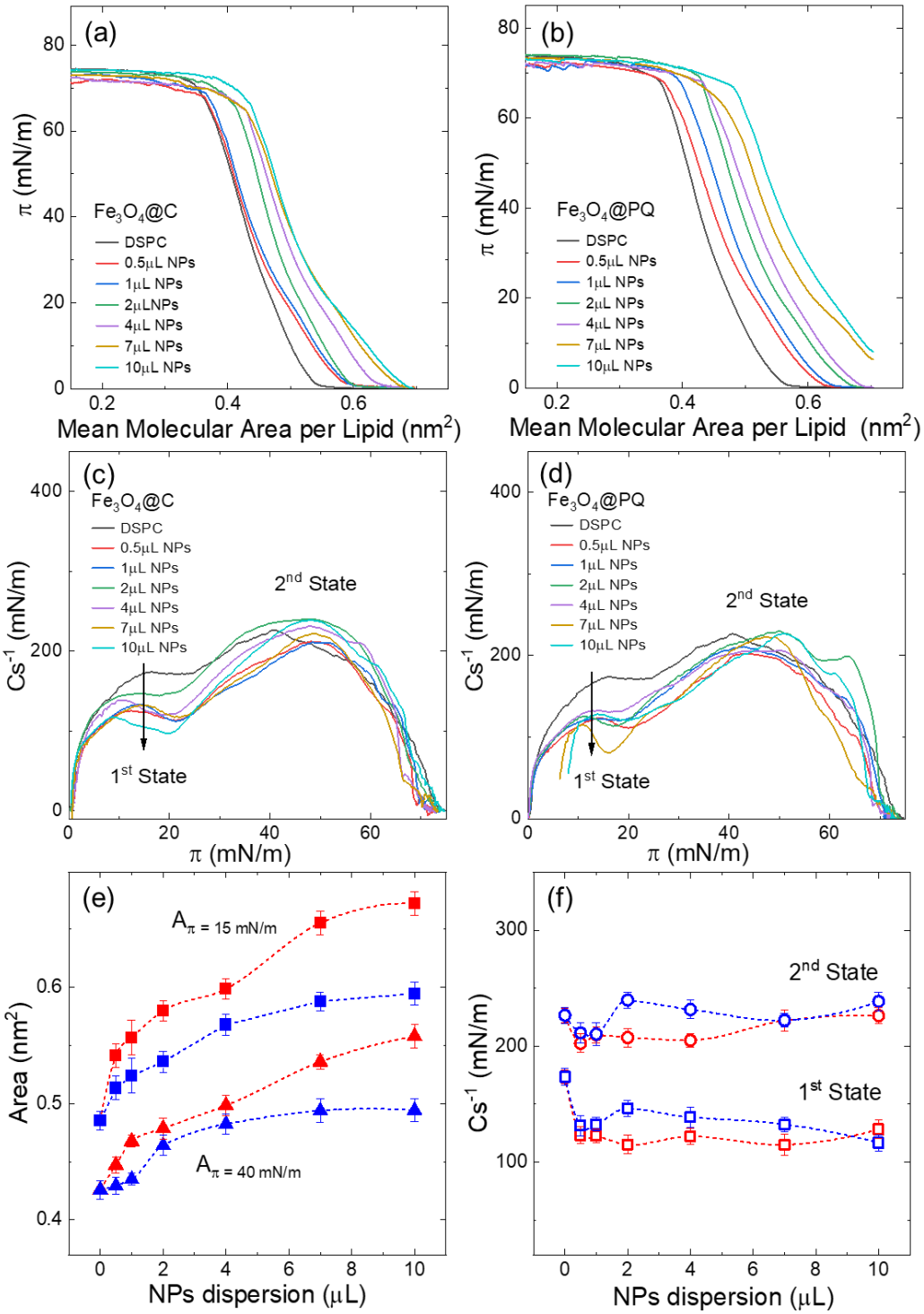

Figure 4. Surface pressure as a function of the mean molecular area per lipid and compressibility modulus for the hybrid films: (a), (c) Fe_3O_4@C/DSPC and (b), (d) Fe_3O_4@PQ/DSPC. (e) Mean molecular area (MMA) as a function of the amount of NPs at two different surface pressures (15 mN/m and 40 mN/m) for Fe_3O_4@C (blue) and Fe_3O_4@PQ (red). (f) Maximum compressibility modulus (Cs^{-1}) of the NP dispersions for Fe_3O_4@C/DSPC (blue) and Fe_3O_4@PQ/DSPC (red) monolayers, in both LE and LC phases. Error bars represent standard deviations from triplicate measurements.

In the case of the hybrid isotherms for Fe_3O_4@PQ/DSPC and Fe_3O_4@C/DSPC, a shift to higher MMA compared to the pure DSPC isotherm is observed. This shift increases monotonically with the amount of NPs in the film. However, the slopes of the isotherms are quite similar to those of the pure DSPC isotherm, indicating that all the films exhibit the same behavior during the compression. The maximum Cs^{-1} value is not significantly affected by the presence of NPs, suggesting that the state of the DSPC monolayer remains unchanged (Figure 4(c), (d), and (f)).

In the isotherm of the Fe_3O_4@C/DSPC film formed with lower NPs concentrations (0.5 and 1.0 µL), changes in shape are observed only during the initial stage of the surface pressure increase. However, at higher surface pressures, the isotherms nearly overlap, suggesting that the NPs are weakly adsorbed onto the DSPC monolayer at the beginning of compression, and further compression leads to squeezing the NPs out of the DSPC monolayer. Similar behavior was observed by Piosik et al. when aminated chitosan-coated Fe_3O_4 NPs interact with DSPC monolayers.[16] At higher NP concentrations, all the isotherms shift to higher MMA values. In addition to the shift in the isotherms generated from the phospholipid-NP mixtures, another noticeable difference is the appearance of a plateau at approximately 15 mN/m. It is also observed as a minimum in the Cs^{-1} graphs. This suggests that a reorganization process occurs at this surface pressure.

Comparing the NPs with both types of covering, Fe_3O_4@PQ induce greater changes in the isotherm of pure DSPC than Fe_3O_4@C, as reflected in more pronounced shifts of the isotherms to higher MMA values (Figure 4(b)). Even at NP concentrations of 0.5 and 1.0 µL, an increase in surface pressure is observed before compression begins. Fe_3O_4@PQ interacts more extensively into the preformed monolayer than Fe_3O_4@C, due to hydrophobic interactions between the cellulose chain and the phospholipid hydrocarbon chains. Since DSPC is a zwitterionic lipid and the surface charge of the NPs is relatively low, electrostatic effects do not play a dominant role in the greater interaction of Fe_3O_4@PQ with the monolayer.

As observed for the NPs/DSPA hybrid films shown in Figure S3(a) and (b) of the Supplementary Information, the isotherms shift toward larger molecular areas only when a small amount of NPs (2 microliters) is injected at the water/air interface. However, with larger amounts of NPs in the interface, the isotherms shift to areas even smaller than those of the pure DSPA isotherm. This behavior suggests that either the NPs are expelled toward the subphase, dragging along some DSPA molecules, or that the formation of aggregates at the interface occurs through the adsorption of DSPA molecules on the NPs surface.[25]

The effect of performing experiments with aged NPs was also analyzed, including aged dispersions (stored for approximately six months) to evaluate the impact of long-term storage on interfacial behavior. Interestingly, despite intense sonication prior to use, these aged suspensions exhibited signs of irreversible aggregation, likely due to magnetic interactions overcoming the stabilizing effect of the surface coating. The effect of NPs from an aged solution on DSPC monolayers is shown in Figures S4(a) and (b) of the Supplementary Information. The addition of increasing amounts of NPs (both Fe_3O_4@C and Fe_3O_4@PQ) results in a systematic rightward shift of the isotherms, indicating an expansion of the monolayer and an increase in the molecular area per lipid at equivalent surface pressures. This shift suggests that the NPs interfere with the lateral packing of DSPC molecules, likely inserting into or associating with the film and thereby disrupting DSPC-DSPC interactions. Also, a plateau region is observed at around 20mN/m, implying changes in the phase behavior and elasticity of the lipid matrix upon NP incorporation. Furthermore, the surface pressure decreases as the amount of NPs in the films increases, which was not observed using fresh NP solutions.

Moreover, a decrease in Cs^{-1} is observed at all surface pressures for both hybrid films (NPs/DSPA or NPs/DSPC), showing that the

films become more compressible and less rigid in the presence of the nanoparticles, and that the film behaves more like an expanded liquid phase, with loosely packed molecules that respond more readily to compression (Figures S3(c), S3(d), S4(c), and 4(d)).

Overall, the modifications observed in the isotherms of lipid monolayers are more pronounced when aged NP solutions are used. Due to their magnetic nature, these particles tend to agglomerate over time, resulting in aged dispersions that behave similarly to larger NPs than those initially synthesized. This highlights the critical importance of using freshly prepared NP solutions in biomedical applications, where consistency in nanoparticle size and dispersion is essential for reproducibility and efficacy.

Brewster angle microscopy (BAM)

Brewster angle microscopy (BAM) studies were conducted to confirm the presence of NPs in the membranes and to evaluate their effect on the morphology of DSPA and DSPC monolayers. Figure 5 displays representative images obtained for DSPA, Fe_3O_4@C/DSPA, and Fe_3O_4@PQ/DSPA monolayers, while the corresponding images for DSPC, Fe_3O_4@C/DSPC, and Fe_3O_4@PQ/DSPC are provided in the Supplementary Information (Figure S5). BAM images of the mixed monolayers (NPs/phospholipids) were recorded using the lowest NP proportion (0.5 μL). The surface pressure values at which BAM micrographs were captured are indicated on the left side of each image. Throughout the compression process of both lipidic and hybrid monolayers, regions with different grayscale intensities are observed, reflecting variations in the molecular packing density.

The images obtained for the DSPA monolayer reveal the presence of lipidic regions in the liquid-condensed (LC) phase (light gray areas) at $\pi = 0$, while the black areas correspond either to gas-phase regions of the monolayer or to interfacial zones devoid of lipid molecules. As compression progresses ($\pi > 1$ mN/m), the LC regions coalesce, forming a uniform film throughout the entire surface pressure range studied ($\pi = 10–50$ mN/m). This behavior, also observed in the DSPC monolayer (Figure S5), is characteristic of phospholipids that form condensed monolayers, where strong van der Waals interactions between hydrocarbon chains lead to densely packed molecular arrangements.[17,26]

On the other hand, BAM images of the Fe_3O_4@C/DSPA and Fe_3O_4@PQ/DSPA hybrid monolayers show bright spots due to the presence of small NP aggregates forming three-dimensional structures. These NP aggregates reflect the incident light more intensely than the phospholipid-covered areas, appearing as bright spots, a phenomenon previously reported for Fe_3O_4 particles.[51] This indicates that the presence of both kinds of NPs in the DSPA monolayer delays the coalescence of LC domains. However, this delay occurs at higher surface pressures for citrate-coated NPs compared to PQ-coated ones, suggesting differences in how each coating interacts with the lipid monolayer. A similar behavior has been previously reported for Fe_3O_4 NPs functionalized with chitosan, where the presence of these NPs in the subphase prevents the coalescence of LC domains in a DSPA monolayer, even at surface pressures up to 11 mN/m.[25]

Finally, as the surface pressure increases in both hybrid monolayers, the gas-phase regions or areas devoid of lipid molecules gradually disappear, leaving only a homogeneous liquid-condensed (LC) phase containing nanoparticle aggregates.

In the case of the hybrid films Fe_3O_4@C/DSPC and Fe_3O_4@PQ/DSPC (Figure S5), a similar behavior is observed. However, the main difference is that lipid-free regions are only present at $\pi = 0$ mN/m in the hybrid film Fe_3O_4@PQ/DSPC. As the surface pressure increases, the LC phase persists along with the NP aggregates at all studied surface pressure values for both systems.

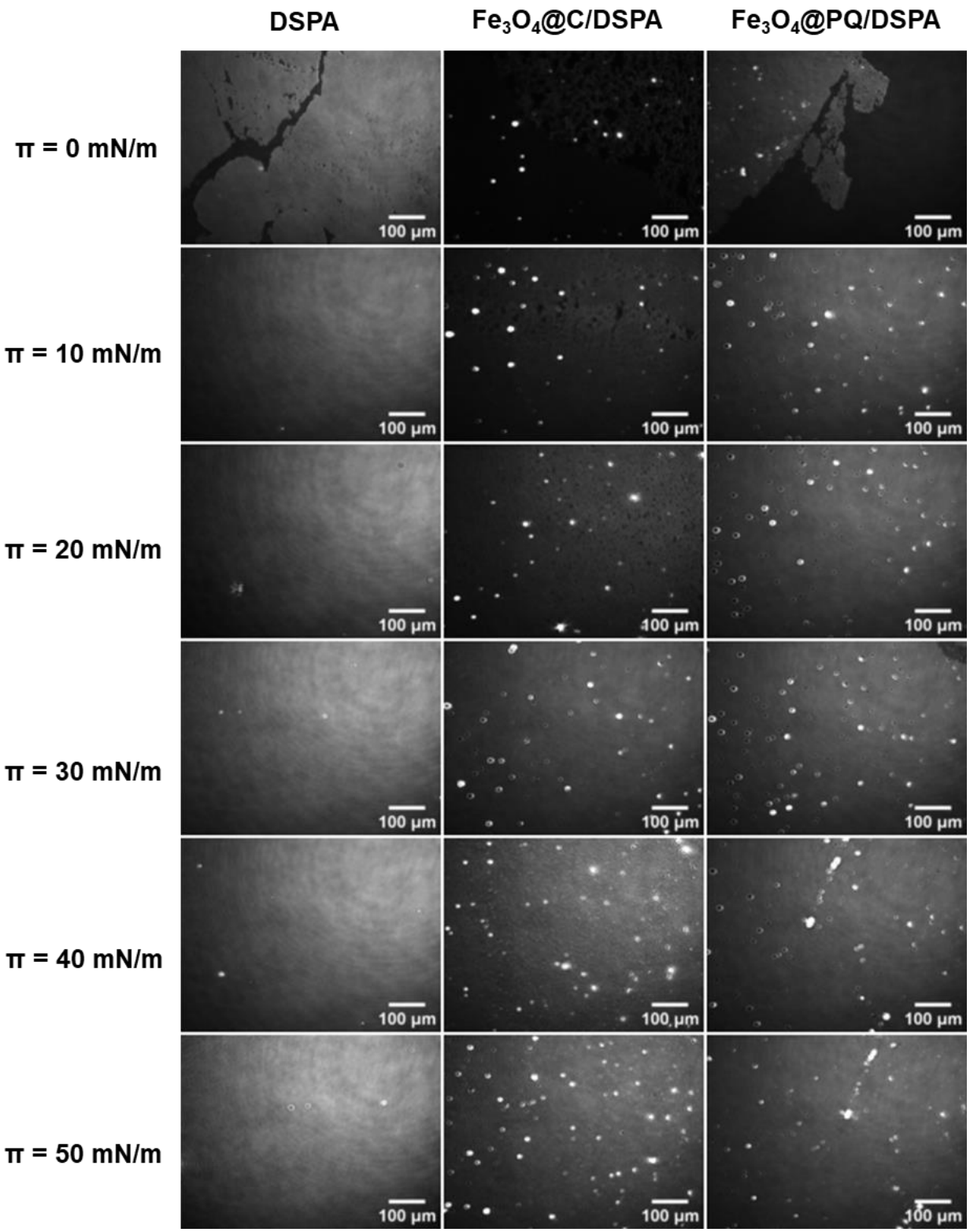

Figure 5. Brewster angle images at different surface pressures for DSPA and 0.5 µL NPs/DSPA hybrid monolayer. The images correspond to the Langmuir isotherm shown in Figures 4 (a) and (b).

From BAM images, the mean gray level values of all the zones observed in the images were quantified. Then, the reflectivity RP of monolayers can be determined by the change of the gray level of a film with and without NPs.[26]

As shown in Figure 6, DSPA and DSPC exhibit a condensed monolayer in the entire range of surface pressures studied, which explains the monotonous behavior of RP, with a constant value of approximately 3x10-6 for both phospholipids.

Despite being immersed in the condensed phospholipid zone, Fe3O4@PQ does not disrupt the ordered state of the lipid hydrocarbon chains, as indicated by the unaltered RP values shown in Figure 6.[54] This finding supports previous observations that these NPs primarily interact from the subphase, facing difficulty in penetrating the monolayer and thus causing minimal disruption to the lateral interactions between hydrocarbon chains.

In contrast, Fe_3O_4@C, previously described as capable of deeper penetration into the phospholipid film, disturbs the lateral packing of the phospholipid chains, leading to structural disorganization. This disruption is evidenced by a noticeable decrease in reflectivity values, which persists even at high surface pressures, as shown in Figure 6.

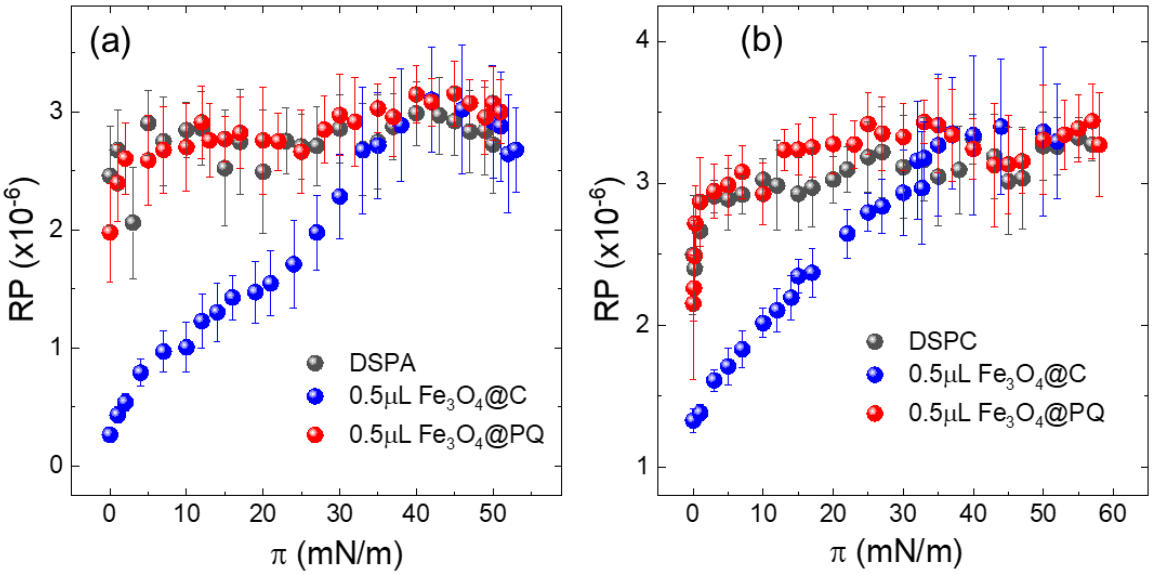

Figure 6. Reflected intensity values (RP) at different surface pressures for: (a) DSPA, NPs/DSPA and (b) DSPC, NPs/DSPC.

Insertion of Fe_3O_4@C and Fe_3O_4@PQ in DSPA and DSPC preformed monolayer

A key parameter for evaluating the interaction of magnetite NPs and preformed monolayers is the saturation concentration, defined as the point at which no further increase in surface pressure is observed, despite the addition of more NPs. Figures S6(a) and (b) in the Supplementary Information display the time-dependent surface pressure profiles following successive injections of NPs into the subphase beneath DSPA and DSPC monolayers, respectively. From these plots, the change in surface pressure ($\Delta\pi$) was plotted against the final NP concentration in the subphase, as shown in Figure 7(a) and (b). Both resulting curves exhibit a hyperbolic trend, which were accordingly fitted using Equation (2). The corresponding fitting parameters are summarized in Table 1.

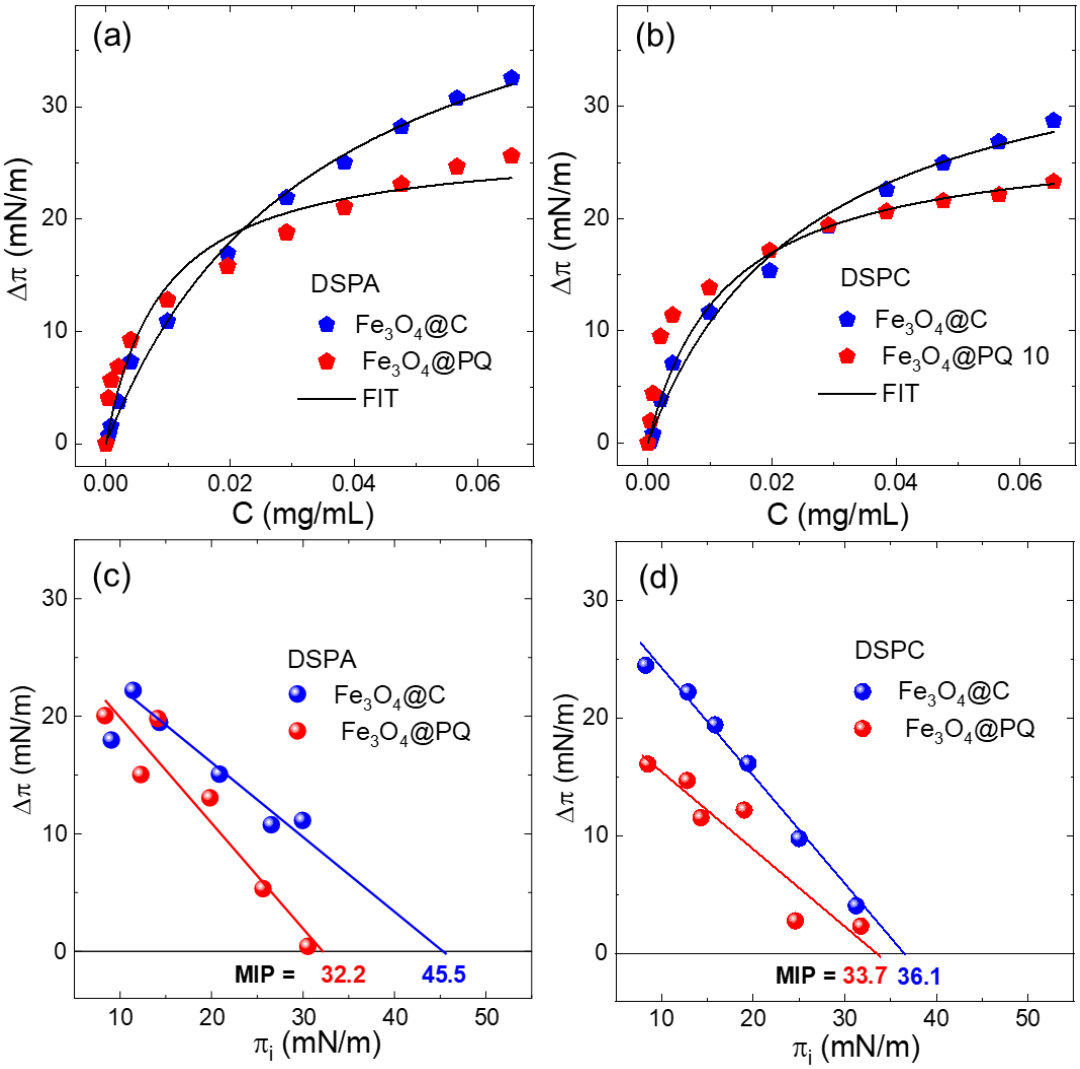

Figure 7. Change in surface pressure (Δπ) as a function of the final NP concentration for monolayers of (a) DSPA and (b) DSPC, π_i = 15 mN/m; the straight line corresponds to a hyperbolic fit. Δπ as a function of the monolayer's initial pressure for (c) DSPA and (d) DSPC; the x-axis intersection of the tangent provides the MIP value. Subphase composition: LiCl 10 mM, pH = 6.0.

The values in Table 1 indicate that Fe_3O_4@C induces greater changes in surface pressure than Fe_3O_4@PQ in both DSPA and DSPC monolayers at the highest concentrations tested. However, the $K_{0.5}$ values, which represent the concentration required to induce 50% of the maximum surface pressure change, were lower for Fe_3O_4@PQ than for Fe_3O_4@C in both monolayers. Therefore, Fe_3O_4@PQ interacts more readily with the monolayers at lower concentrations but reaches saturation more quickly. This behavior may be attributed to the initial interaction between the hydrophobic cellulose chains of the PQ coating and the phospholipid tails, facilitating early insertion. However, the smaller size of Fe_3O_4@C may favor deeper incorporation into the monolayer once initial contact occurs. Furthermore, the negative surface charge of Fe_3O_4@C could initially hinder its interaction with the polar phospholipid heads, but once this electrostatic barrier is overcome, the NPs penetrate the monolayer more effectively, ultimately producing greater changes in surface pressure.

Table 1. Values of $\Delta\pi_{max}$ and $K_{0.5}$ obtained from hyperbolic fitting. MIP (maximum insertion pressure) values obtained from Δπ versus π_i plots.

Sample	$\Delta\pi_{max}$ (mN/m)	$K_{0.5}$ (μg/mL)	MIP (mN/m)
Fe_3O_4@C/DSPA	49 ± 2	35 ± 4	46 ± 6
Fe_3O_4@PQ/DSPA	29 ± 2	11 ± 3	32 ± 6
Fe_3O_4@C/DSPC	39 ± 3	26 ± 4	36 ± 3
Fe_3O_4@PQ/DSPC	28 ± 1	12 ± 2	34 ± 7

After establishing how the NPs penetration varies with concentration, we evaluated the influence of DSPA and DSPC monolayer packing on NP incorporation. For this, a fixed amount of each nanoparticle type (250 μL of a solution 0.05 mg/mL) was injected beneath monolayers prepared at different initial surface pressures (π_i). In all cases, a marked increase in surface pressure was observed upon NP injection, as shown in Figure S7, in the Supplementary Information. Over time, the surface pressure reached a plateau, indicating that the system had reached equilibrium and confirming the incorporation of Fe_3O_4@C and Fe_3O_4@PQ into the monolayers. This figure also shows how the net change in surface pressure (Δπ) is determined.

The plots of Δπ versus π_i for the preformed DSPA and DSPC monolayers are shown in Figure 7(c) and (d), respectively, where it can be observed that lower initial surface pressures (π_i) lead to a greater net increase in surface pressure (Δπ). This behavior is expected since incorporation into expanded monolayers is energetically more favorable. Conversely, at higher π_i values, meaning more condensed monolayers, the observed changes in surface pressure are smaller, indicating reduced NP incorporation.

In all the studied systems, the maximum insertion pressure (MIP) values exceed 30 mN/m, suggesting that these NPs could incorporate into model membranes with packing densities comparable to biological membranes. Although biological membranes do not exhibit surface pressure as defined in Langmuir monolayers, lateral pressure ranges of 20–35 mN/m are commonly used in model systems to mimic membrane organization.[6] Notably, the results also show that, regardless of the phospholipid type, Fe_3O_4@C NPs induce a greater Δπ, indicating more effective incorporation compared to Fe_3O_4@PQ.

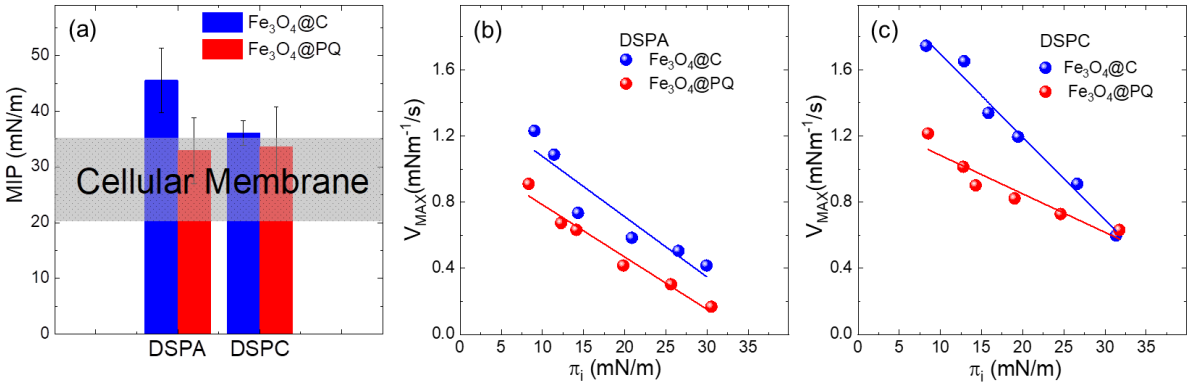

Figure 8. (a) Maximum insertion pressure (MIP). Maximum penetration rates (V_{MAX}) for: (b) Fe_3O_4@C/DSPA (blue) and Fe_3O_4@PQ/DSPA (red), and (c) Fe_3O_4@C/DSPC (blue) and Fe_3O_4@PQ/DSPC (red).

Figure 8(a) summarizes the MIP values for the different NPs. In every case, the MIP values exceeded the lateral pressure range typically used to approximate cell membrane conditions, represented by the gray band between 20–35 mN/m.

Reiner *et. al.* reported that the time–dependent penetration rate (V_{MAX}) can be obtained for all π_i from the maximum of the first derivative of π–time plots.[55] Figure 8(b) and (c) present the V_{MAX} values as a function of π_i for DSPA and DSPC monolayers, respectively. In both cases, a clear decreasing trend is observed: as π_i increases, the insertion rate of the NPs decreases. This behavior suggests that magnetite NPs incorporation is more favorable in less condensed monolayers, in agreement with the trends observed in the $\Delta\pi$–π_i plots shown in Figure 7. In addition, in both hybrid films, higher V_{MAX} values were observed for Fe_3O_4@C NPs.

To complement this analysis, the experimental π–time curves were fitted using a pseudo-first-order kinetic model (Equation 3), which allowed determining the rate constant *k* for each condition studied. As expected, *k* decreases progressively with increasing π_i, confirming that the kinetic resistance to NP insertion increases with monolayer packing. This trend was consistent across both lipid types and NP coatings. The fitting procedure and representative curves are shown in Figure S8, and the corresponding parameters are summarized in Table S1 (Supporting Information). The observed decrease in the rate constant *k* with increasing π_i is in agreement with the V_{max} profiles presented in Figure 8, further supporting that monolayer packing density strongly influences NP insertion dynamics.

CONCLUSION

Fe_3O_4@C and Fe_3O_4@PQ NPs were successfully synthesized and characterized. FTIR and zeta potential analyses confirmed effective surface functionalization, while magnetic measurements revealed superparamagnetic behavior with reduced saturation magnetization due to non-magnetic surface layers. The coatings preserved the particle size and morphology, which was confirmed by TEM, while maintaining the magnetite crystal structure, as shown by XRD.

Inclusion of magnetite NPs significantly affects the thermodynamic behavior of DSPA and DSPC lipid monolayers. The NPs with both types of covering expand the monolayer at low concentrations due to area exclusion effects but lead to reduced MMAs at higher concentrations, due to NP aggregation and the formation of 3D structures. Aged NP solutions caused more pronounced disruptions and decreased the film rigidity, emphasizing the need for fresh magnetite NP dispersions in applications, to ensure consistent behavior and reproducibility.

BAM confirmed Fe_3O_4@C and Fe_3O_4@PQ NPs incorporation into DSPA and DSPC monolayers. While pure DSPA and DSPC formed uniform and condensed films upon compression, hybrid monolayers exhibited delayed domain coalescence and the appearance of bright aggregates due to NP clustering. Notably, Fe_3O_4@C induced greater disruption in lipid packing, as evidenced by decreased reflectivity values, indicating deeper integration into the monolayer. In contrast, Fe_3O_4@PQ showed minimal impact on the condensed lipid structure, suggesting limited insertion and interaction primarily from the subphase.

Insertion studies demonstrated that Fe_3O_4@C and Fe_3O_4@PQ interact with preformed DSPA and DSPC monolayers, being their incorporation governed by NP concentration and monolayer packing. Fe_3O_4@PQ NPs insert more readily at lower concentrations, whereas Fe_3O_4@C NPs induce greater surface pressure changes at saturation, suggesting deeper integration into the lipid matrix. Additionally, $\Delta\pi$–π_i, V_{MAX}–π_i and *k*–π_i profiles confirmed that NP insertion is more favorable in expanded monolayers. Notably, all systems displayed MIP values above 30 mN/m, exceeding physiological membrane pressures, indicating that both NP shells have the potential to penetrate biological membranes. Upon all conditions evaluation, Fe_3O_4@C exhibited

superior insertion efficiency and higher V_{MAX} and *k* values, highlighting the critical influence of surface chemistry on monolayer interaction dynamics. Overall, magnetite NPs modulate lipid film packing, elasticity, and stability depending on concentration, type, and age of the NPs.

ASSOCIATED CONTENT

Supporting Information

XRD measurements of NPs, Figure SI1. NP isotherms, Figure SI2. The influence of using aged NP solutions evaluated by isotherms and compressibility modulus (Figure SI4). Brewster angle images at different surface pressures for DSPC and 0.5 μL NPs/DSPC hybrid monolayer (Figure SI5). Insertion of Fe_3O_4@C and Fe_3O_4@PQ on DSPA and DSPC pre-formed monolayer, Figure S6 and S7. Kinetic analysis of NP insertions into monolayers, Figure S8.

ACKNOWLEDGMENTS

This work was partially supported by Secyt-UNC and Conicet PIP 11220200102625CO projects. Viviana Daboin acknowledges a doctoral fellowship from Conicet.

REFERENCES

(1) Khan, A. U.; Chen, L.; Ge, G. Recent Development for Biomedical Applications of Magnetic Nanoparticles. *Inorg. Chem. Commun.* **2021**, *134*, 108995. https://doi.org/10.1016/j.inoche.2021.108995.

(2) Andrada, H. E.; Venosta, L. F.; Jacobo, S. E.; Silva, O. F.; Falcone, R. D.; Bercoff, P. G. Highly Stable Nanostructured Magnetic Vesicles as Doxorubicin Carriers for Field-assisted Therapies. *ChemNanoMat.* **2022**, *8* (4), 1–13. https://doi.org/10.1002/cnma.202100409.

(3) Atrei, A.; Mahdizadeh, F. F.; Baratto, M. C.; Scala, A. Effect of Citrate on the Size and the Magnetic Properties of Primary Fe_3O_4 Nanoparticles and Their Aggregates. *Appl. Sci.* **2021**, *11*, 6974. https://doi.org/10.3390/app11156974.

(4) Ziegler-Borowska, M.; Chełminiak, D.; Kaczmarek, H. Thermal Stability of Magnetic Nanoparticles Coated by Blends of Modified Chitosan and Poly(quaternary Ammonium) Salt. *J. Therm. Anal. Calorim.* **2015**, *119*, 499–506. https://doi.org/10.1007/s10973-014-4122-7.

(5) Nowak-Jary, J.; Machnicka, B. Pharmacokinetics of Magnetic Iron Oxide Nanoparticles for Medical Applications. *J. Nanobiotechnol.* **2022**, *20*, 305. https://doi.org/10.1186/s12951-022-01510-w.

(6) Ábrahám, N.; Csapó, E.; Bohus, G.; Dékány, I. Interaction of Biofunctionalized Gold Nanoparticles with Model Phospholipid Membrane. *Colloid Polym. Sci.* **2014**, *292*, 2715. https://doi.org/10.1007/s00396-014-3302-0.

(7) Wilke, N. Lipid Monolayers at the Air–Water Interface: A Tool for Understanding Electrostatic Interactions and Rheology in Biomembranes. *Adv. Planar Lipid Bilayers Liposomes.* **2014**, *2*, 51–81. https://doi.org/10.1016/B978-0-12-418698-9.00002-2.

(8) Nobre, T. M.; Pavinatto, F. J.; Caseli, L.; Barros-Timmons, A.; Dynarowicz-Łątka, P.; Oliveira, O. N., Jr. Interactions of Bioactive Molecules and Nanomaterials with Langmuir Monolayers as Cell Membrane Models. *Thin Solid Films.* **2015**, *593*, 158–188. https://doi.org/10.1016/j.tsf.2015.09.047.

(9) Sarkis, J.; Vié, V. Biomimetic Models to Investigate Membrane Biophysics Affecting Lipid–Protein Interaction. *Front. Bioeng. Biotechnol.* **2020**, *8*, 207. https://doi.org/10.3389/fbioe.2020.00270.

(10) Cámara, C. I.; Riva, J. S.; Juárez, A. V.; Yudi. L. M. Interaction of chitosan and self-assembled distearoylphosphatidic acid molecules at liquid/liquid and air/water interfaces. Effect of temperature. *J. Phys. Org. Chem.* **2016,** *29*, 672-681. https://doi.org/10.1002/poc.3642

(11) Krajewska, M.; Dopierała, K.; Prochaska. K. Lipid–Protein Interactions in Langmuir Monolayers under Dynamically Varied

Conditions. *J. Phys. Chem. B.* **2020,** *124*, 302, https://doi.org/10.1021/acs.jpcb.9b10351.
(12) Pereira, A. R.; Fiamingo, A.; Pedro, R. de O.; Campana-Filho, S. P.; Miranda, P. B.; Oliveira Jr., O. N. Enhanced Chitosan Effects on Cell Membrane Models Made with Lipid Raft Monolayers. *Colloids Surf., B.* **2020**, *193*, 111017. https://doi.org/10.1016/j.colsurfb.2020.111017.
(13) Nobre, T. M.; Pavinatto, F. J.; Caseli, L.; Barros-Timmons, A.; Dynarowicz-Łątka, P.; Oliveira Jr., O. N. Langmuir Films Containing Ibuprofen and Phospholipids. *Chem. Phys. Lett.* **2013**, *559*, 99–106. https://doi.org/10.1016/j.cplett.2012.12.064.
(14) Moya Betancourt, S. N.; Cámara, C. I.; Riva, J. S. Interaction between Pharmaceutical Drugs and Polymer-Coated Fe_3O_4 Magnetic Nanoparticles with Langmuir Monolayers as Cellular Membrane Models. *Pharmaceutics.* **2023**, *15*, 311. https://doi.org/10.3390/pharmaceutics15020311.
(15) Guzmán, E.; Santini, E.; Ferrari, M.; Liggieri, L.; Ravera, F. Interaction of Particles with Langmuir Monolayers of 1,2-Dipalmitoyl-sn-Glycero-3-Phosphocholine: A Matter of Chemistry? *Coatings.* **2020**, *10*, 469. https://doi.org/10.3390/coatings10050469.
(16) Piosik, E.; Klimczak, P.; Ziegler-Borowska, M.; Chełminiak-Dudkiewicz, D.; Martyński, T. A. Detailed Investigation on Interactions between Magnetite Nanoparticles Functionalized with Aminated Chitosan and a Cell Model Membrane. *Mater. Sci. Eng., C.* **2020**, *109*, 110616. https://doi.org/10.1016/j.msec.2019.110616.
(17) Piosik, E.; Ziegler-Borowska, M.; Chełminiak-Dudkiewicz, D.; Martynski, T. Effect of Aminated Chitosan-Coated Fe_3O_4 Nanoparticles with Applicational Potential in Nanomedicine on DPPG, DSPC, and POPC Langmuir Monolayers as Cell Membrane Models. *Int. J. Mol. Sci.* **2021**, *22*, 2467. https://doi.org/10.3390/ijms22052467.
(18) Guzmán, E.; Santini, E.; Ferrari, M.; Liggieri, L.; Ravera, F. Effect of the Incorporation of Nanosized Titanium Dioxide on the Interfacial Properties of 1,2-Dipalmitoyl-sn-Glycerol-3-Phosphocholine Langmuir Monolayers. *Langmuir*. **2017**, *33*, 10715–10725. https://doi.org/10.1021/acs.langmuir.7b02484.
(19) Lins, P. M. P.; Marangoni, V. S.; Uehara, T. M.; Miranda, P. B.; Zucolotto, V.; Cancino-Bernardi, J. Differences in the Aspect Ratio of Gold Nanorods That Induce Defects in Cell Membrane Models. *Langmuir*. **2017**, *33*, 14286–14294. https://doi.org/10.1021/acs.langmuir.7b03051.
(20) Cancino-Bernardi, J.; Lins, P. M. P.; Marangoni, V. S.; Faria, H. A. M.; Zucolotto, V. Difference in lipid cell composition and shaped-based gold nanoparticles induce distinguish pathways in Langmuir monolayers response. *Mater. Today Commun.* **2021**, *26*, 101831. https://doi.org/10.1016/j.mtcomm.2020.101831.
(21) Tim, B.; Rojewska, M.; Prochaska, K. Effect of silica microparticles on interactions in mono- and multicomponent membranes. *Int. J. Mol. Sci.* **2022**, *23*, 12822.https://doi.org/10.3390/ijms232112822.
(22) Piosik, E.; Modlinska, A.; Gołaszewski, M.; Chełminiak-Dudkiewicz, D.; Ziegler-Borowska, M. Influence of the type of biocompatible polymer in the shell of magnetite nanoparticles on their interaction with DPPC in two-component Langmuir monolayers. *J. Phys. Chem. B.* **2024**, *128*, 781–794.
(23) Moya Betancourt, S. N.; Cámara, C. I.; Juarez, A. V.; Pozo López, G.; Riva, J. S. Effect of magnetic nanoparticles coating on their electrochemical behaviour at a polarized liquid/liquid interface. *J. Electroanal. Chem.* **2022**, *911*, 116253.
(24) Moya Betancourt, S. N.; Uranga, J. G.; Cámara, C. I.; Juarez, A. V.; Pozo López, G.; Riva, J. S. Effect of bare and polymeric-modified magnetic nanoparticles on the drug ion transfer across liquid/liquid interfaces. *J. Electroanal. Chem.* **2022**, *919*, 116502.
(25) Moya Betancourt, S. N.; Riva, J. S. Opposite effects produced by MNPs: phospholipid films generated at a liquid/liquid

interface, in the drug transfer processes. *Electrochim. Acta.* **2023**, *433*, 141967. https://doi.org/10.1016/j.electacta.2023.141967.
(26) Moya Betancourt, S. N.; Cámara, C. I.; Juarez, A. V.; Riva, J. S. Magnetically controlled insertion of magnetic nanoparticles into membrane models. *Biochim. Biophys. Acta, Biomembr.* **2024**, *1866*, 184293.K.L.
(27) Bierbrauer, K. L.; Alasino, R. V.; Strumia, M. C.; Beltramo, D. M. Cationic cellulose and its interaction with chondroitin sulfate: rheological properties of the polyelectrolyte complex. *Eur. Polym. J.* **2014**, *50*, 142–149.
(28) Riva, J. S.; Bierbrauer, K.; Beltramo, D.; Yudi, L. M. Electrochemical study of the behaviour of cationic polyelectrolytes, and their complexation with monovalent anionic surfactants. *Electrochim. Acta.* **2012**, *85*, 659–664.
(29) Qureashi, A.; Pandith, A. H.; Bashir, A.; Manzoor, T.; Malik, L. A.; Sheikh, F. A. Citrate coated magnetite: a complete magneto dielectric, electrochemical and DFT study for detection and removal of heavy metal ions. *Surf. Interfaces.* **2021**, *23*, 101004. https://doi.org/10.1016/j.surfin.2021.101004.
(30) Sreeja, V.; Joy, P. A. Effect of inter-particle interactions on the magnetic properties of magnetite nanoparticles after coating with dextran. *Int. J. Nanotechnol.* **2011**, *8*, 907–915. https://doi.org/10.1504/IJNT.2011.044435.
(31) Yang, D.; Hu, J.; Fu, S. Controlled synthesis of magnetite–silica nanocomposites via a seeded sol-gel approach. *J. Phys. Chem. C.* **2009**, *113*, 7646–7651. https://doi.org/10.1021/jp900868d.
(32) Cámara, C. I.; Crosio, M. A.; Juarez, A. V.; Wilke, N. Dexamethasone and dexamethasone phosphate: effect on DMPC membrane models. *Pharmaceutics.* **2023**, *15*, 844.https://doi.org/10.3390/pharmaceutics15030844.
(33) Moya, S. N.; Cámara, C. I.; Riva, J. S. Interaction between pharmaceutical drugs and polymer-coated Fe_3O_4 magnetic nanoparticles with Langmuir monolayers as cellular membrane models. *Pharmaceutics.* **2023**, *15*, 311. https://doi.org/10.3390/pharmaceutics15020311.
(34) Hao, C.; Li, J.; Mu, W.; Zhu, L.; Yang, J.; Liu, H.; Li, B.; Chen, S.; Sun, R. Adsorption Behavior of Magnetite Nanoparticles into the DPPC Model Membranes. *Appl. Surf. Sci.* **2016**, 362, 121–125. https://doi.org/10.1016/j.apsusc.2015.11.173.
(35) Mottola, M.; Perillo, M. A.; Caruso, B. Langmuir Films at the Oil/Water Interface Revisited. *Sci. Rep*. **2019**, *9*, 38674. https://doi.org/10.1038/s41598-019-38674-9.
(36) Daboin, V. B.; Moya, S. N.; Farias, E. D.; Riva, J. S.; Bercoff, P. G. Enhancement of the electrochemical oxygen evolution reaction by light and external magnetic fields, using hybrid electrodes made by Langmuir–Blodgett. *Electrochim. Acta.* **2024**, *480*, 143910. https://doi.org/10.1016/j.electacta.2024.143910.
(37) Bui, T. Q.; Ton, S. N.; Duong, A. T.; Tran, H. T. Size-dependent magnetic responsiveness of magnetite nanoparticles synthesized by co-precipitation and solvothermal methods. *J. Sci.: Adv. Mater. Devices.* **2018**, *3*, 107–112. https://doi.org/10.1016/j.jsamd.2017.11.002
(38) Pham, X. N.; Nguyen, T. P.; Pham, T. N.; Tran, T. T. N.; Tran, T. V. T. Synthesis and characterization of chitosan-coated magnetite nanoparticles and their application in curcumin drug delivery. *Adv. Nat. Sci.: Nanosci. Nanotechnol.* **2016**, *7*, 045010. https://doi.org/10.1088/2043-6262/7/4/045010.
(39) Qureashi, A.; Pandith, A. H.; Bashir, A.; Manzoor, T.; Malik, L. A.; Sheikh, F. A. Citrate Coated Magnetite: A Complete Magneto Dielectric, Electrochemical and DFT Study for Detection and Removal of Heavy Metal Ions. *Surf. Interfaces.* **2021**, *23*, 101004. https://doi.org/10.1016/j.surfin.2021.101004.
(40) Yang, D.; Hu, J.; Fu, S. Controlled Synthesis of Magnetite-Silica Nanocomposites via a Seeded Sol-Gel Approach. *J. Phys. Chem. C.* **2009**, *113*, 7646–7651. https://doi.org/10.1021/jp900868d.

(41) Nigam, S.; Barick, K. C.; Bahadur, D. Development of Citrate-Stabilized Fe_3O_4 Nanoparticles: Conjugation and Release of Doxorubicin for Therapeutic Applications. *J. Magn. Magn. Mater.* **2011**, *323*, 237–243. https://doi.org/10.1016/j.jmmm.2010.09.009.
(42) Ramalingam, B.; Khan, M. M.; Mondal, B.; Mandal, A. B.; Das, S. K. Facile Synthesis of Silver Nanoparticles Decorated Magnetic-Chitosan Microsphere for Efficient Removal of Dyes and Microbial Contaminants. *ACS Sustainable Chem. Eng.* **2015**, *3*, 2291–2302. https://doi.org/10.1021/acssuschemeng.5b00577.
(43) Sharma, G.; Park, S.; Bandi, R.; Ahn, J.; Alle, M.; Kim, J. Polyquaternium Enhances the Colloidal Stability of Chitosan-Capped Platinum Nanoparticles and Their Antibacterial Activity. *Nanotechnology.* **2021**, *32*, 455603. https://doi.org/10.1088/1361-6528/ac1afa.
(44) Fekry, M.; Elmesallamy, S. M.; El-Rahman, N. R. A.; Bekhit, M.; Elsaied, H. A. Eco-Friendly Adsorbents Based on Abietic Acid, Boswellic Acid, and Chitosan/Magnetite for Removing Waste Oil from the Surface of the Water. *Environ. Sci. Pollut. Res.* **2022**, *29*, 64633–64646. https://doi.org/10.1007/s11356-022-20169-2.
(45) Maity, D.; Agrawal, D. C. Synthesis of Iron Oxide Nanoparticles under Oxidizing Environment and Their Stabilization in Aqueous and Non-Aqueous Media. *J. Magn. Magn. Mater.* **2007**, *308*, 46–55. https://doi.org/10.1016/j.jmmm.2006.05.001.
(46) Daboin, V. B.; Riva, J. S.; Bercoff, P. G. Magnetic Behavior of Nanofilms Prepared by Assembling Different Co. *Mater. Res. Bull.* **2025**, *184*, 113229. https://doi.org/10.1016/j.materresbull.2024.113229.
(47) Daboin, V. B.; Riva, J. S.; Bercoff, P. G. Magnetic Nanofilms Prepared by Langmuir–Blodgett Nanoarchitectonics Using Co and Co–Y Ferrite Nanoparticles. *Mater. Res. Bull.* **2025**, *189*, 113449. https://doi.org/10.1016/j.materresbull.2025.113449.
(48) Zhang, H.; Zeng, D.; Liu, Z. The Law of Approach to Saturation in Ferromagnets Originating from the Magnetocrystalline Anisotropy. *J. Magn. Magn. Mater.* **2010**, *322*, 2375–2380. https://doi.org/10.1016/j.jmmm.2010.02.040.
(49) Davies, J. T.; Rideal, S. E. K. *Interfacial Phenomena*; Academic Press: New York, 1963.
(50) Moghaddam, B.; Ali, M. H.; Wilkhu, J.; Kirby, D. J.; Mohammed, A. R.; Zheng, Q.; Perrie, Y. The Application of Monolayer Studies in the Understanding of Liposomal Formulations. *Int. J. Pharm.* **2011**, *417*, 235–244. https://doi.org/10.1016/j.ijpharm.2011.01.020.
(51) Zhao, L.; Feng, S. S. Effects of Lipid Chain Unsaturation and Headgroup Type on Molecular Interactions between Paclitaxel and Phospholipid within Model Biomembrane. *J. Colloid Interface Sci.* **2005**, *285*, 326–335. https://doi.org/10.1016/j.jcis.2004.11.032.
(52) Zhao, L.; Feng, S. S. Effects of Lipid Chain Length on Molecular Interactions between Paclitaxel and Phospholipid within Model Biomembranes. *J. Colloid Interface Sci.* **2004**, *274*, 55–68. https://doi.org/10.1016/j.jcis.2003.12.009.
(53) Lee, D. K.; Kim, Y. H.; Kim, C. W.; Cha, H. G.; Kang, Y. S. Vast Magnetic Monolayer Film with Surfactant-Stabilized Fe_3O_4 Nanoparticles Using Langmuir–Blodgett Technique. *J. Phys. Chem. B.* **2007**, *111*, 9288–9293. https://doi.org/10.1021/jp072612c.
(54) Roldán-Carmona, C.; Giner-Casares, J. J.; Pérez-Morales, M.; Martín-Romero, M. T.; Camacho, L. Revisiting the Brewster Angle Microscopy: The Relevance of the Polar Headgroup. *Adv. Colloid Interface Sci.* **2012**, *173*, 12–22. https://doi.org/10.1016/j.cis.2012.02.002.
(55) Reiner, G. N.; Perillo, M. A.; García, D. A. Langmuir Monolayers as a Model to Study the Interaction of Drugs with Membranes. *Colloids Surf. B.* **2013**, *101*, 61–67. https://doi.org/10.1016/j.colsurfb.2012.06.004.

Suplementary Information

NPs characterization

The crystal structure was determined using X-ray powder diffraction (XRD) with a PANalytical X'Pert Pro diffractometer, operated in Bragg-Brentano geometry at 40 kV and 40 mA, using Cu Kα radiation (λ = 1.5418 Å) with a step size of 0.02° over a scanning range of 10° to 80°. The X-ray diffraction patterns of Fe_3O_4, Fe_3O_4@C, and Fe_3O_4@PQ are presented in Figure S1. In all the samples, the peak positions corresponding to the (111), (220), (311), (400), (422), (511), and (440) reflections match the standard diffraction peaks of the cubic spinel structure, characteristic of magnetite (JCPDS 00-019-0629).

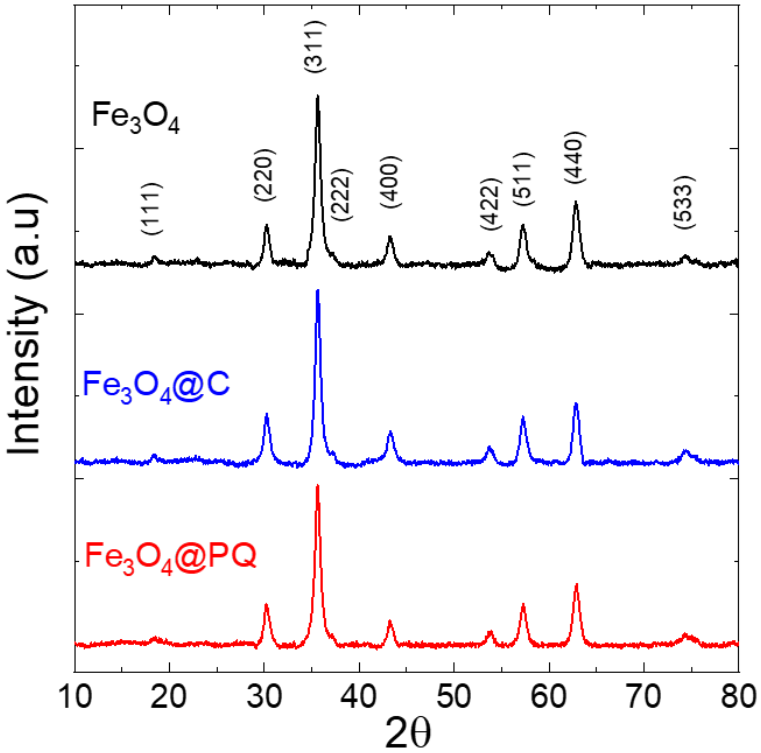

Figure S1. XRD patterns of Fe_3O_4, Fe_3O_4@C, and Fe_3O_4@PQ nanoparticles.

Surface Pressure–Mean Molecular Area Isotherms

Figure S2 shows the compression isotherms of the Langmuir layers formed by 60μL of NPs in a chloroform suspension. Upon compression of the monolayer, a notable increase in surface pressure is observed, reaching a value close to 25 mN/m for Fe_3O_4@PQ, and close to 17 mN/m for Fe_3O_4@C, values that will be referred to as the critical pressure (π_c) of the nanoparticle film. For Fe_3O_4@PQ NPs, a change in slope is observed at around 12 mN/m, indicating a reorganization process of the nanoparticles on the surface.

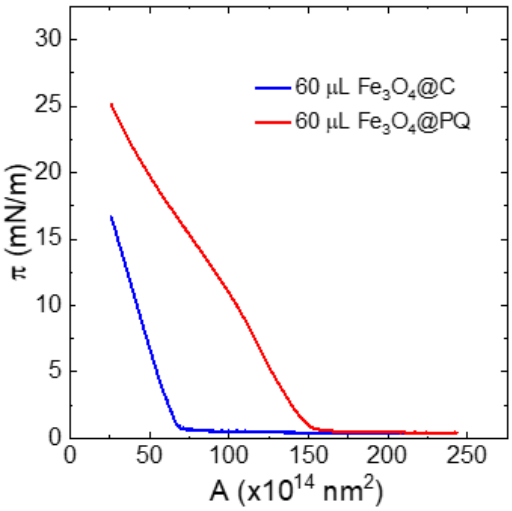

Figure S2. Surface pressure as a function of the area for Fe_3O_4@C and Fe_3O_4@PQ bare nanoparticles.

The influence of using an aged NP solution was also evaluated. As shown in Figures S3(a) and S3(b), for Fe_3O_4@NPs/DSPA hybrid monolayers, the compression isotherms shift toward larger molecular areas only when a small volume (2 µL) of NPs is deposited at the air/water interface. In contrast, at higher NP concentrations, the isotherms shift toward smaller molecular areas compared to that of the pure DSPA monolayer. This behavior suggests two possible mechanisms: (i) the expulsion of NPs into the subphase, accompanied by partial removal of DSPA molecules, or (ii) the formation of interfacial aggregates through adsorption of DSPA onto the nanoparticle surface.

The effect of aged NPs on DSPC monolayers is illustrated in Figures S4(a) and S4(b). Upon increasing the amount of NPs (Fe_3O_4@C and Fe_3O_4@PQ), a systematic shift of the isotherms toward higher molecular areas is observed, indicating monolayer expansion and disruption of lipid packing. This expansion reflects interference with DSPC–DSPC lateral interactions, likely due to nanoparticle insertion or association at the interface. Additionally, a plateau is evident near 20 mN/m, indicative of modifications in phase transitions and elastic properties of the lipid matrix induced by nanoparticle incorporation.

Furthermore, the compressibility modulus (Cs^{-1}) decreases across all surface pressures for both hybrid systems (Fe_3O_4@NPs/DSPA and Fe_3O_4@NPs/DSPC), as shown in Figures S3(c), S3(d), S4(c), and S4(d). This decrease reflects increased compressibility and reduced rigidity of the monolayers in the presence of NPs, suggesting that the film adopts a more expanded, liquid-like state characterized by loosely packed molecules that respond more readily to lateral compression.

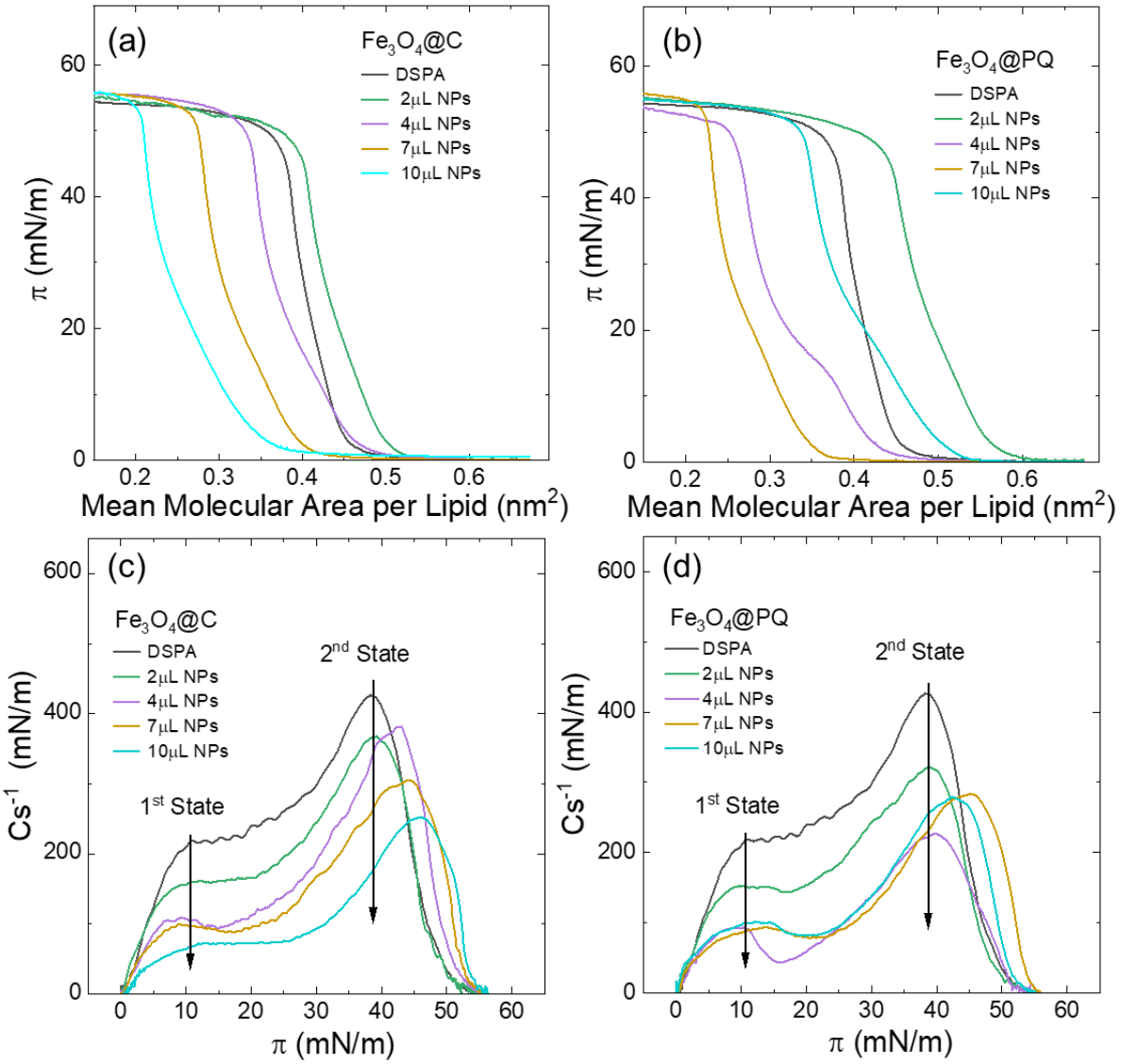

Figure S3. Surface pressure as a function of the mean molecular area per lipid and compressibility modulus for the mixtures: (a), (c) Fe_3O_4@C/DSPA and (b), (d) Fe_3O_4@PQ/DSPA.

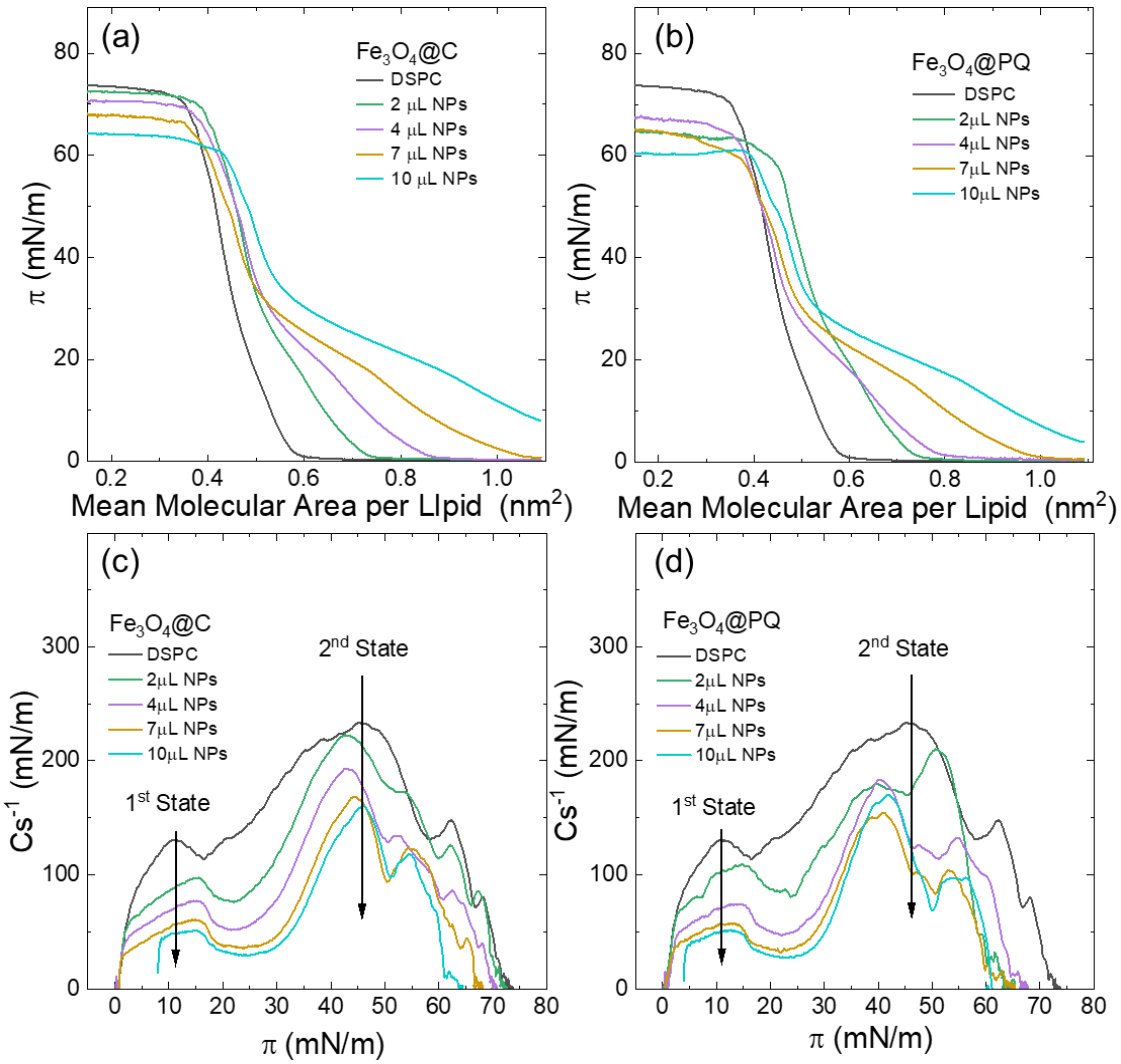

Figure S4. Surface pressure as a function of the mean molecular area per lipid and compressibility modulus for the mixtures: (a), (c) Fe_3O_4@C/DSPC and (b), (d) Fe_3O_4@PQ/DSPC.

Brewster angle microscopy (BAM)

Figure S5 shows the BAM images recorded during the compression of DSPC and the hybrid films with the minimum ratio of NPs (0.5 μL). The BAM images captured for the DSPC monolayer show the presence of extensive blocks of lipid molecules in the LC state, except at a pressure of π = 0 mN/m. Also, for NPs/DSPC hybrid films at π = 0 mN/m, bright spots are observed, due to the presence of small NO aggregates in the monolayer. For this type of hybrid film, the presence of black zones without lipid molecules is only detected at a surface pressure equal to 0 mN/m in the presence of Fe_3O_4@PQ particles.

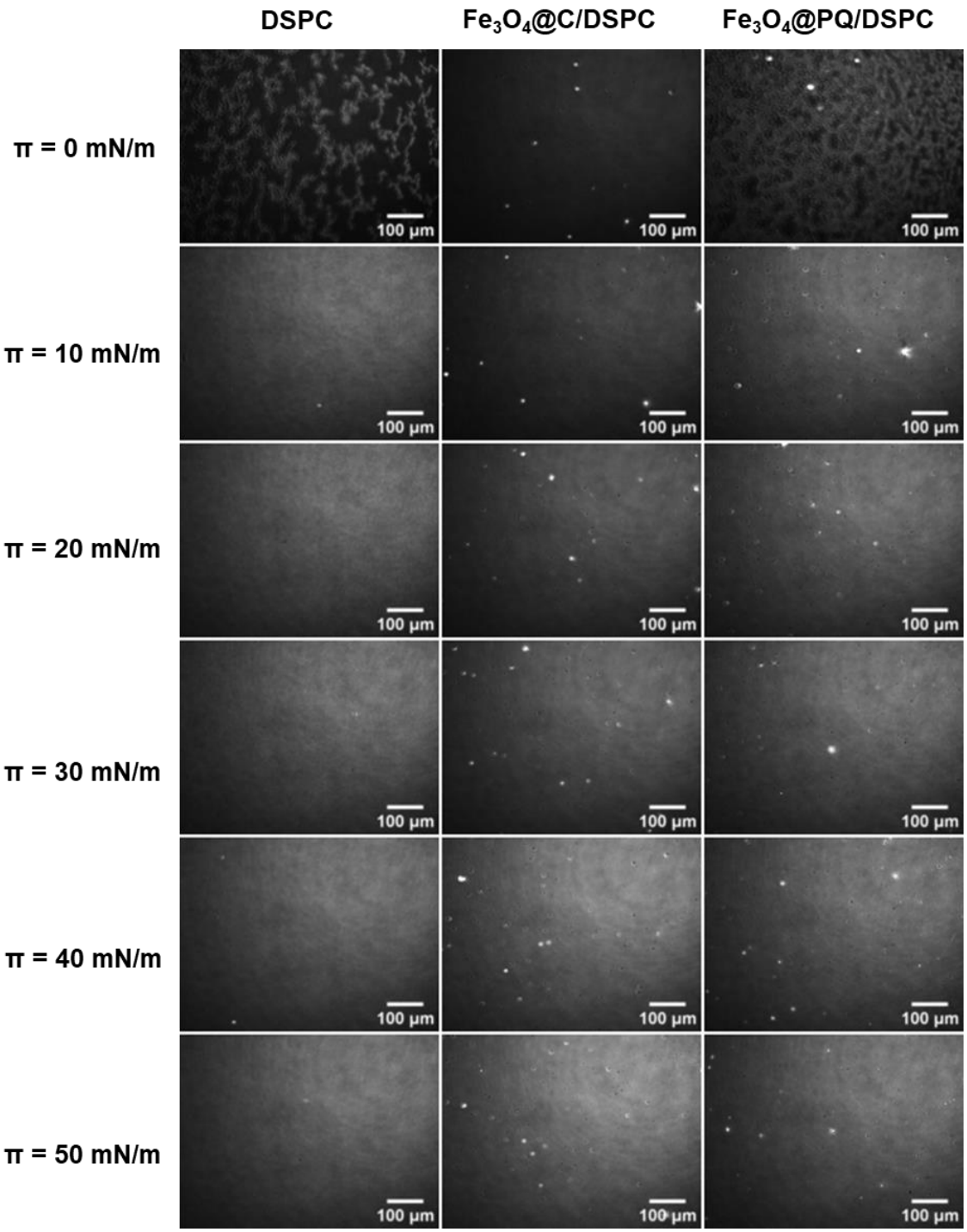

Figure S5. Brewster angle images at different surface pressures for DSPC and 0.5 µL NPs/DSPC hybrid monolayer. The images correspond to the Langmuir isotherm shown in Figure 4. (a) and (b).

Insertion of Fe_3O_4@C and Fe_3O_4@PQ on DSPA and DSPC preformed monolayer

An essential parameter for analyzing the interaction between NPs and preformed monolayers is the saturation concentration. This point is defined by the absence of further increases in surface pressure, even when additional NPs are introduced.

In order to obtain the saturation concentration, a DSPA or DSPC phospholipid monolayer with a surface pressure equal to 15 mN/m was made at the surface of 10 mM NaCl subphase. Subsequently, additive volumes of NPs dispersion were injected into the subphase until reaching the maximum concentration at which no further changes in surface pressure were observed. This value was 0.05 mg/mL or 250 µL of each NPs, and corresponds to the saturation concentration. This concentration of the NPs was used in the adsorption experiments to determine the value of the maximum insertion pressure (MIP).

Figures S6 (a) and (b) show the changes in surface pressure over time as successive NP concentrations were injected from the subphase into preformed DSPA and DSPC monolayers, respectively. From these plots, the dependence of surface pressure on the final NP concentration which is injected into the subphase was determined for both monolayers.

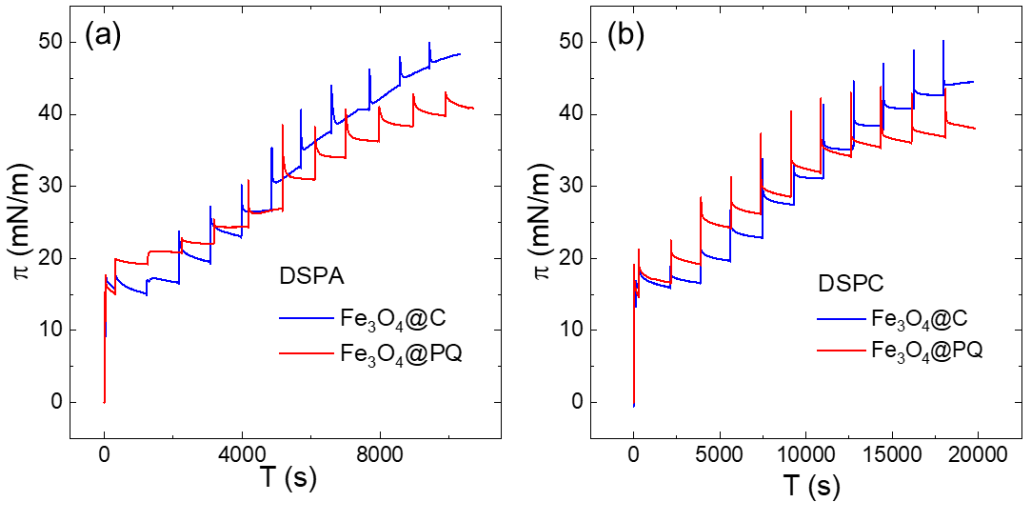

Figure S6. Successive NP dispersions injections into monolayers of (a) DSPA or (b) DSPC.

Figures S7 (a) and (b) show the change of surface pressure with time, when the NPs are injected on the surface, starting from various initial surface pressures, π_i of the preformed DSPA and DSPC monolayer

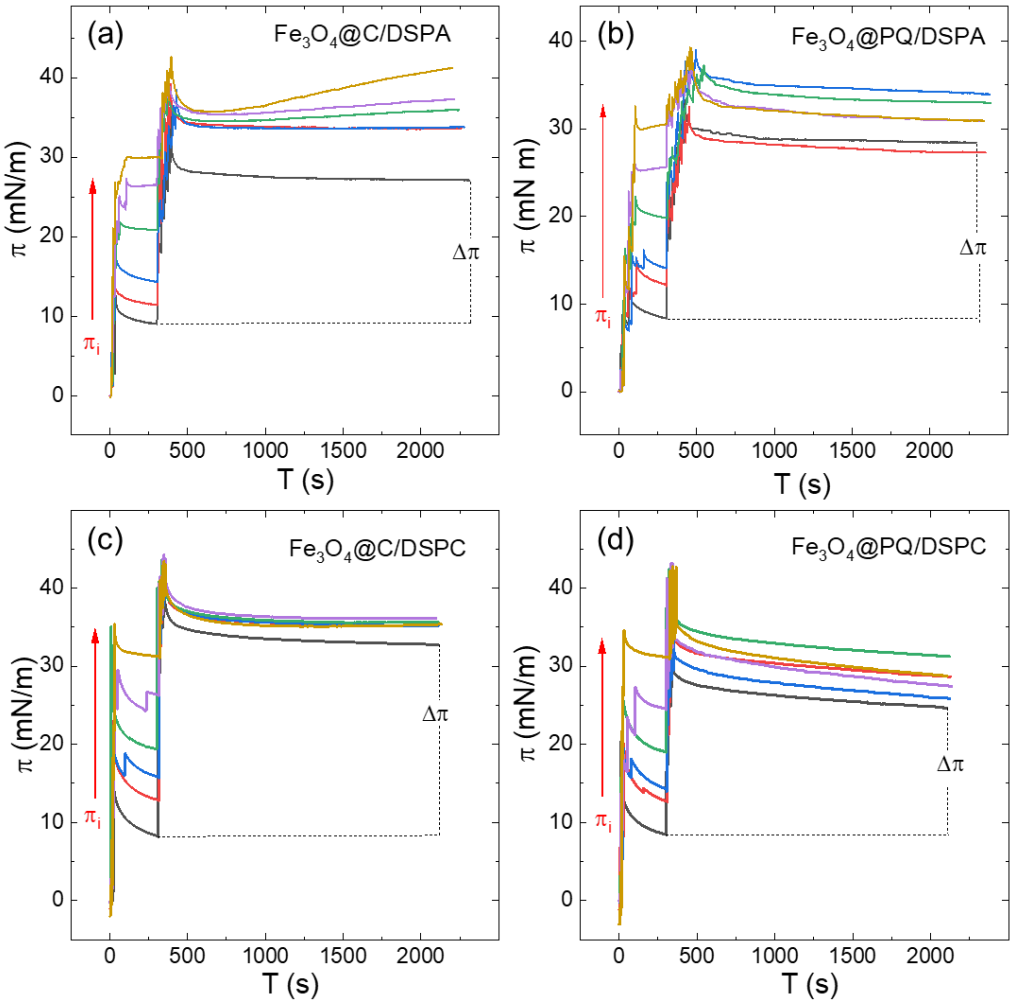

Figure S7. Change in surface pressure as a function of time after the injection of (a) Fe_3O_4@C/DSPA, (b) Fe_3O_4@PQ/DSPA, (c) Fe_3O_4@C/DSPC, and (d) Fe_3O_4@PQ/DSPC.

Figure S8 shows the kinetic analysis of nanoparticle insertion into DSPA and DSPC monolayers. Figure S8 (a) displays a representative surface pressure versus time curve obtained after Fe_3O_4@C nanoparticle injection at an initial surface pressure of approximately 15 mN/m, along with its fit using the first-order kinetic model described by the next equation (Equation 3 in the manuscript):

$$\pi(t) = \pi_0 + \Delta\pi_{max}(1 - e^{-kt})$$

The quality of the fit indicates that the model provides an adequate description of the insertion kinetics under the conditions studied.

Figures S8 (b) and (c) present the rate constants k (s^{-1}) obtained by the fitting, as a function of the initial surface pressure (π_i) for Fe_3O_4@C and Fe_3O_4@PQ nanoparticles interacting with DSPA and DSPC monolayers, respectively. In all cases, k decreases as π_i increases, indicating that insertion becomes progressively slower as the lipid monolayer becomes more densely packed. This kinetic trend complements the behavior observed in $\Delta\pi$ and V_{max} analyses. Table S1 lists the fitting parameters obtained from Equation 3 for each system and initial surface pressure.

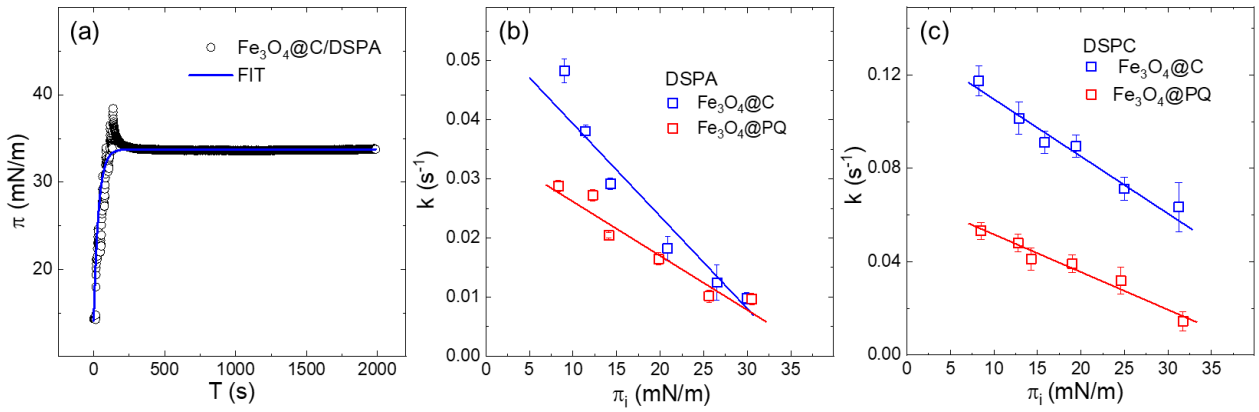

Figure S8. (a) Representative fitting of the surface pressure versus time curve using the pseudo-first-order kinetic model (Equation 3), for a DSPA monolayer with an initial surface pressure of approximately 15 mN/m after Fe_3O_4@C nanoparticle injection. Rate constant k (s^{-1}) as a function of initial surface pressure (π_i) for Fe_3O_4@C and Fe_3O_4@PQ nanoparticles interacting with (b) DSPA and (c) DSPC monolayers.

Table S1. Fitting parameters obtained from the fitting of surface pressure versus time curves using the first-order kinetic model (Equation 3). $\Delta\pi_{max}$ represents the amplitude of the surface pressure increase, k is the pseudo-first-order rate constant (s^{-1}), and π_0 is the initial surface pressure prior to NP injection.

Fe_3O_4@C/DSPA			**Fe_3O_4@PQ/DSPA**		
π_0 (mN/m)	**$\Delta\pi_{max}$ (mN/m)**	**k (s^{-1})**	**π_0 (mN/m)**	**$\Delta\pi_{max}$ (mN/m)**	**k (s^{-1})**
9.35 ± 0.38	17.89 ± 0.38	0.050 ± 0.002	8.02 ± 0.25	20.82 ± 0.25	0.029 ± 0.001
11.04 ± 0.27	22.82 ± 0.27	0.038 ± 0.001	12.02 ± 0.30	15.56 ± 0.29	0.027 ± 0.001
14.15 ± 0.31	19.63 ± 0.21	0.029 ± 0.001	14.19 ± 0.29	20.22 ± 0.29	0.020 ± 0.001
20.81 ± 0.32	14.35 ± 0.31	0.018 ± 0.003	19.82 ± 0.28	13.25 ± 0.28	0.017 ± 0.001
26.43 ± 0.32	9.85 ± 0.32	0.012± 0.003	25.57 ± 0.36	6.47 ± 0.35	0.010 ± 0.001
29.99 ± 0.43	7.39 ± 0.42	0.009 ± 0.001	30.04 ± 0.30	1.62 ± 0.29	0.009 ± 0.001
Fe_3O_4@C/DSPC			**Fe_3O_4@PQ/DSPC**		
π_0 (mN/m)	**$\Delta\pi_{max}$ (mN/m)**	**k (s^{-1})**	**π_0 (mN/m)**	**$\Delta\pi_{max}$ (mN/m)**	**k (s^{-1})**
8.14 ± 0.91	24.60 ± 0.91	0.117 ± 0.007	8.42 ± 0.78	16.71 ± 0.77	0.053 ± 0.004
12.86 ± 0.72	22.29 ± 0.72	0.101 ± 0.007	12.49 ± 0.87	16.18 ± 0.86	0.048 ± 0.004
15.63 ± 0.71	19.75 ± 0.67	0.091 ± 0.005	14.04 ± 0.97	11.97 ± 0.97	0.041 ± 0.005
19.53 ± 0.59	16.39 ± 0.59	0.089 ± 0.005	19.04 ± 0.80	12.22 ± 0.80	0.039 ± 0.004
26.16 ± 0.48	10.37 ± 0.48	0.071 ± 0.005	24.43 ± 0.62	3.17 ± 0.80	0.032 ± 0.006
31.32 ± 0.48	4.02 ± 0.48	0.063 ± 0.011	31.38 ± 0.59	1.16 ± ± 0.59	0.015 ± 0.004

Table of Contents (TOC) Graphic